








RESEARCH ARTICLE | APRIL 07 2022

Graphics processing unit accelerated lattice Boltzmann method simulations of dilute gravity currents

Damilola Adekanye ; Amirul Khan ; Alan Burns ; William McCaffrey ; Martin Geier ; Martin Schönherr ; Robert Dorrell 



Physics of Fluids 34, 046602 (2022)

<https://doi.org/10.1063/5.0082959>

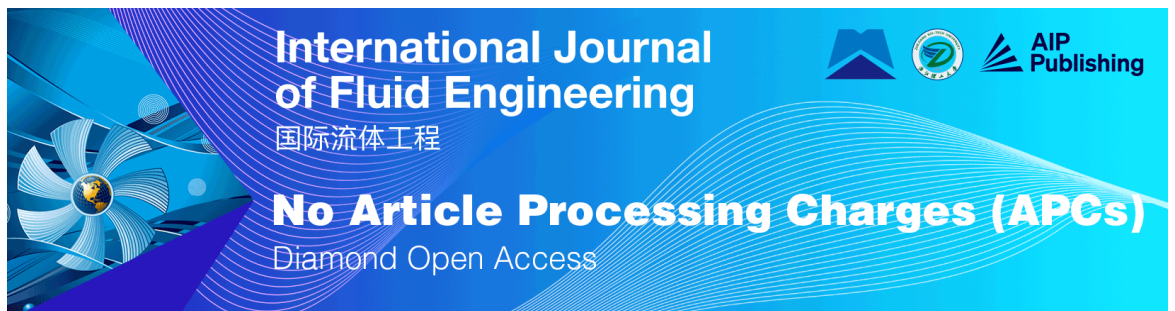


View
Online




Export
Citation

CrossMark



**International Journal
of Fluid Engineering**
国际流体工程

No Article Processing Charges (APCs)
Diamond Open Access



Graphics processing unit accelerated lattice Boltzmann method simulations of dilute gravity currents

Cite as: Phys. Fluids **34**, 046602 (2022); doi: 10.1063/5.0082959

Submitted: 20 December 2021 · Accepted: 7 February 2022 ·

Published Online: 7 April 2022



View Online



Export Citation



CrossMark

Damilola Adekanye,^{1,a)} Amirul Khan,² Alan Burns,³ William McCaffrey,⁴ Martin Geier,⁵ Martin Schönherr,⁵ and Robert Dorrell⁶

AFFILIATIONS

¹EPSRC Centre for Doctoral Training in Fluid Dynamics, School of Computing, University of Leeds, Leeds LS2 9JT, United Kingdom

²School of Civil Engineering, University of Leeds, Leeds LS2 9JT, United Kingdom

³School of Chemical and Process Engineering, University of Leeds, Leeds LS2 9JT, United Kingdom

⁴School of Earth and Environment, University of Leeds, Leeds LS2 9JT, United Kingdom

⁵Institute for Computational Modelling in Civil Engineering, TU Braunschweig, Pockelsstr. 3, 38106 Brunswick, Germany

⁶Energy and Environment Institute, University of Hull, Hull HU6 7RX, United Kingdom

^{a)}Author to whom correspondence should be addressed: damilolaadekanye@gmail.com

ABSTRACT

Lattice Boltzmann method models offer a novel framework for the simulation of high Reynolds number dilute gravity currents. The numerical algorithm is well suited to acceleration via implementation on massively parallel computer architectures. Here, we present two lattice Boltzmann method models of lock-exchange dilute gravity currents in which the largest turbulent length scales are directly resolved. The three-dimensional simulations are accelerated by exporting computations to a graphics processing unit and are validated against experiments and high-resolution simulations for Reynolds numbers up to 30 000. The lattice Boltzmann method models achieve equivalent accuracy to conventional large-eddy simulation models in the prediction of key flow properties. A conservative analysis of computational performance relative to conventional methods indicates that the presented framework reduces simulation times by two orders of magnitude. Therefore, it can be used as a foundation for the development of depth-resolving models that capture more of the complexity of environmental gravity currents.

© 2022 Author(s). All article content, except where otherwise noted, is licensed under a Creative Commons Attribution (CC BY) license (<http://creativecommons.org/licenses/by/4.0/>). <https://doi.org/10.1063/5.0082959>

NOMENCLATURE

c	Velocity quantum, $c = \Delta x / \Delta t$
c_{ijk}^{Qm}	Discrete set of m velocities in a three-dimensional space where $i, j, k \in \{1, 0, -1\}$
C_{nrs}	Cumulant of order $n + r + s$
C_{nrs}^*	Post-collision cumulant of order $n + r + s$
C_{nrs}^{eq}	Equilibrium cumulant of order $n + r + s$
CPU	Central processing unit
C_s	Smagorinsky constant
c_s	Speed of sound in the lattice
D	Diffusivity of the scalar field
$DnQm$	Defines a lattice structure with n dimensions and m velocities

DNS	Direct numerical simulation
e_{L_1}	L_1 error
e^g	Unit vector in the direction of gravitational acceleration, i.e., $e^g = (0, 0, -1)^T$
f	Continuous particle distribution function
F_B	Boussinesq forcing term
f_{ijk}	Discretized particle distribution function
f_{ijk}^{eq}	Discretized equilibrium particle distribution function
F_w	Total frictional force applied to the lower boundary
F_w^{DNS}	Total frictional force applied to the lower boundary in a DNS simulation
$F_w^{LBM-LES}$	Total frictional force applied to the lower boundary in an LBM-LES simulation
Fr	Froude number

\mathbf{G}	Macroscopic body force acting on the flow	t_{SV}	Time at which a lock-exchange gravity current transitions from the slumping to viscous phase
g	Gravitational acceleration	\mathbf{u}	Macroscopic velocity field $\mathbf{u} = (u, v, w)^T$
g'	Reduced gravity	U_b	Buoyancy velocity
GPU	Graphics processing unit	u_f	Front velocity of the gravity current
H	Channel depth	u_τ	Friction velocity
h_0	Initial current depth	w_{ijk}^{Qm}	A constant set of weights corresponding to m discrete velocities
h_f	Height of the current head	\mathbf{x}	Position in Cartesian coordinate system, that is, $\mathbf{x} = (x, y, z)^T$
L_1	Length of the computational domain in the x direction	x_0	The distance of the lock gate from the start of the channel
L_2	Length of the computational domain in the y direction	x_f	The distance between the current front and the initial lock gate position
L_3	Length of the computational domain in the z direction	z_{\max}^+	The maximum z^+ recorded across all wall-adjacent nodes throughout the duration of the simulation
LBM	Lattice Boltzmann method	z^+	Non-dimensional distance from the wall
LBM-GPU	Lattice Boltzmann method solver that ports computations to a graphics processing unit	α	Coefficient of expansion
LBM-LES	Lattice Boltzmann method model that uses a large eddy simulation turbulence model	Δ	Filter width
LES	Large eddy simulation	Δt	Time step
M_{nrs}	Factorized central moments of order $n + r + s$	Δx	Grid spacing
M_{nrs}^*	Post-collision factorized central moments of order $n + r + s$	Δz_1	Distance from a wall adjacent node to the boundary wall
m_{ABC}	Raw moments of order $A + B + C$	Δz_2	Distance from a wall adjacent node to the nearest node in the wall normal direction
MNUPS	Million node updates per second	$\delta\rho$	The component of fluid density that fluctuates around the mean
N_{L_3}	Number of nodes discretizing the L_3 dimension of the computational domain	κ_{nrs}	Central moments of order $n + r + s$
N_{nodes}	Total number of nodes in the computational domain	ν	Viscosity of the ambient fluid
N_t	Number of timesteps for which a results file was written to the hard drive	ν_T	Local eddy viscosity
NS	Navier–Stokes	ξ	Particle velocity field $\xi = (\xi_x, \xi_y, \xi_z)$
NS-DNS	A method that solves the Navier–Stokes equations and resolves all scales of the turbulent flow	Ξ	Velocity–frequency variable $\Xi = \{\Xi, Y, Z\}$
NS-LES	A method that solves the Navier–Stokes equations and uses a large-eddy simulation turbulence model	ξ_{IP}	Empirical constant that parameterizes the inertial phase scaling law
P	Pressure	ξ_{VP}	Empirical constant that parameterizes the viscous phase scaling law
P_j	A list of n processors, that is, $P_j \in \{P_1, P_2, \dots, P_n\}$.	ρ	Density
p_k	Kinematic pressure	$\bar{\rho}$	Mean density
Re_b	Buoyancy Reynolds number	ρ_0	Initial current density
Re_{cr}	Critical buoyancy Reynolds number	ρ_a	Density of the ambient fluid
\bar{S}	Local stress tensor	ρ_s	Solute density
S_{ijk}	Momentum density source term in the lattice Boltzmann equation	τ	Characteristic relaxation time of the fluid
Sc	Schmidt number	τ_w	Wall shear stress
Sc_T	Turbulent Schmidt number	τ_Φ	Characteristic relaxation time of the scalar field
t	Time	Φ	Continuous particle distribution function for the scalar field
$t_{P_j}^i$	A block of processing time on one of n processors $P_j \in \{P_1, P_2, \dots, P_n\}$	Φ_{ijk}	Discretized particle distribution function for the scalar field
T_{CPU}	Total central processing unit time required to run a simulation	Φ_{ijk}^{eq}	Discretized equilibrium particle distribution function for the scalar field
T_E	Total elapsed time required to run a simulation	χ	Solute concentration
T_{End}	Time at which the simulation is terminated	χ_0	Initial solute concentration in the current
t_i	A list of N_t times at which a results file was output i.e., $t_i \in \{t_1, t_2, \dots, t_{N_t}\}$	χ_a	Solute concentration of the ambient fluid
t_{IV}	Time at which a lock-exchange gravity current transitions from the inertial to viscous phase	Ω	Continuous collision operator
t_{SI}	Time at which a lock-exchange gravity current transitions from the slumping to inertial phase	Ω_{ijk}	Discretized collision operator
		ω_{nrs}	Characteristic relaxation frequency of order $n + r + s$
		$\hat{\text{accent}}$	Indicates that the variable has been non-dimensionalized by the length scale h_0 and the velocity scale $(g'h_0)^{\frac{1}{2}}$

- ˜ accent: Indicates that the variable has been non-dimensionalized by the length scale H and the velocity scale $U_b = (g'H)^{\frac{1}{2}}$
- ¯ accent: Indicates that the variable has been spanwise averaged, i.e., along the L_2 direction

I. INTRODUCTION

Gravity currents are flows driven by the buoyancy forces that arise due to the action of gravity on a density gradient within a fluid. The broad class of environmental buoyancy-driven flows includes thermohaline flows¹ and saline currents,² which are driven by temperature and salt-concentration gradients, respectively. Temperature and salinity gradients can occur simultaneously within a system, resulting in double-diffusive gravity currents.³ Density gradients may also be generated by the suspension of particles within the flow, as is the case in turbidity currents, which are ocean-floor underflows consisting of a dense mixture of fluid and sediment particles.⁴ In the case of turbidity currents, there is the added complexity of the current exchanging particulate material with the boundary through erosion and deposition, resulting in a two-way coupled relationship between the hydrodynamics of the flow and morphodynamics of the channel geometry.^{5,6} Direct observation and measurement of turbidity currents in the environment are rare due to the infrequent and destructive nature of the flow. Therefore, the dynamics are investigated through theoretical, experimental, and numerical modeling. The propagation of gravity currents is of broad interest in environmental fluid dynamics, with relevance to research areas as diverse as the study of ocean current dynamics,⁷ and the development of carbon capture and storage processes.⁸

The lock-exchange saline gravity current experiment is the classical problem used to investigate the dynamics of dilute gravity currents. The conventional experimental setup is illustrated in Fig. 1 and consists of a straight channel of depth H in which a relatively light ambient fluid of density, ρ_a , is separated by a gate from a fluid of density $\rho_0 > \rho_a$, and depth h_0 . In the case of dilute gravity currents, the density difference is small $(\rho_0 - \rho_a)/\rho_a \ll 1$; hence, the Boussinesq approximation can be applied, which assumes density variations are small enough to be neglected in the governing equations unless they are acted on by gravity.⁹ The reduced gravity of the system is defined as $g' = g(\rho_0 - \rho_a)/\rho_a$, where g is acceleration due to gravity.

The gate is placed at a distance x_0 from the start of the channel, and when removed, a gravity current is initiated by the resulting horizontal hydrostatic pressure gradient. The current propagates along the channel, with its front located at a distance $x_f(t)$ from the initial position of the gate (x_0), and at a height $h_f(t)$ above the lower boundary, where t denotes time. The channel depth (H) is taken as the

characteristic length scale of the flow, and the characteristic velocity scale is the buoyancy velocity $U_b = \sqrt{g'H}$. These characteristic scales combine with the viscosity of the ambient fluid (ν) to define the buoyancy Reynolds number, $Re_b = U_b H/\nu$.

Following a brief period of frontal acceleration, lock-exchange gravity currents exhibit three distinct phases: the slumping, inertial, and viscous phases.¹⁰ In the slumping phase, the current front advances at a constant velocity (u_f) under a balance of pressure and drag forces.^{10–13} The Froude number of the current is defined as the non-dimensional front velocity in the slumping phase, $Fr = \frac{u_f}{U_b}$.

In the inertial phase, the flow is governed by a balance of inertial and buoyancy forces. It has been determined, through both theoretical modeling and empirical study, that in the inertial phase front location (x_f) and velocity (u_f) tend asymptotically toward Eqs. (1) and (2), respectively.^{10,14–16} In Eqs. (1) and (2), and throughout this paper, symbols with a \sim above them indicate values non-dimensionalized by the characteristic length scale H , and velocity scale U_b ,

$$\tilde{x}_f = \zeta_{IP} (\tilde{h}_0 \tilde{x}_0)^{\frac{1}{3}} t^{\frac{2}{3}}, \tag{1}$$

$$\tilde{u}_f = \frac{2}{3} \zeta_{IP} (\tilde{h}_0 \tilde{x}_0)^{\frac{1}{3}} t^{-\frac{1}{3}}. \tag{2}$$

The viscous phase is governed by the balance of viscous and buoyancy forces. Hoult¹⁵ derived a self-similarity solution of the depth-averaged Navier-Stokes equations to determine the viscous spreading rate of oil slicks on the surface of freshwater. Huppert¹⁷ completed a similar analysis for the case of a dense viscous underflow over a no-slip boundary, which bears a closer relation to the lock-exchange problem, arriving at the scaling laws in the following equations:

$$\tilde{x}_f = \zeta_{VP} (\tilde{h}_0^3 \tilde{x}_0^3 Re_b) ^{\frac{1}{5}} t^{\frac{1}{5}}, \tag{3}$$

$$\tilde{u}_f = \frac{1}{5} \zeta_{VP} (\tilde{h}_0^3 \tilde{x}_0^3 Re_b) ^{\frac{1}{5}} t^{-\frac{4}{5}}. \tag{4}$$

The empirical constant ζ_{IP} was originally set to $\zeta_{IP} = 1.6$ by Hoult¹⁵ and $\zeta_{IP} = 1.47$ by Huppert and Simpson.¹⁰ Huppert¹⁷ set the viscous phase constant to $\zeta_{VP} = 1.13$. The values of the empirical constants were revised by Cantero *et al.*,¹⁸ who fit the ζ_{IP} and ζ_{VP} using a range of experimental and numerical results, ultimately arriving at the best fit values of $\zeta_{IP} = 1.47$ and $\zeta_{VP} = 3.2$.

The time of transition between the phases can be determined by equating the scaling laws.¹⁸ Doing so results in the transition from the slumping to inertial phase occurring at \tilde{t}_{SI} , the transition from

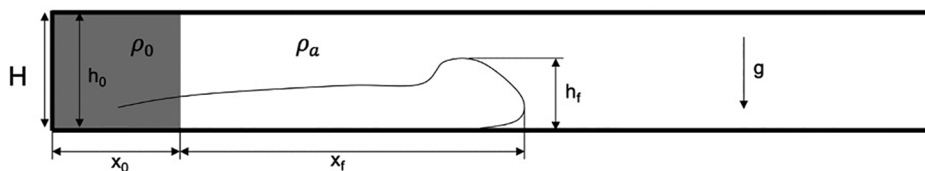


FIG. 1. Lock-exchange gravity current parameters.

slumping to viscous occurring at \tilde{t}_{SV} , and the inertial to viscous phase transition occurring at \tilde{t}_{IV} , as shown in Eqs. (5)–(8), respectively. In the event that $\tilde{t}_{SV} < \tilde{t}_{SI}$, the flow will transition straight from the slumping to viscous phase and bypass the inertial phase entirely. The parameterization of the constants ξ_{IP} and ξ_{VP} , conducted by Cantero *et al.*,¹⁸ had the effect of fitting the phase transition times predicted by the scaling laws to empirical data. The critical Reynolds number, above which the inertial phase develops, can be found by equating Eqs. (5) and (6), giving Eq. (8),

$$\tilde{t}_{SI} = \left(\frac{2\xi_{IP}}{3Fr}\right)^3 \tilde{h}_0 \tilde{x}_0, \tag{5}$$

$$\tilde{t}_{SV} = \left(\frac{1}{5}\xi_{VP}\right)^{\frac{5}{4}} \frac{(\tilde{h}_0 \tilde{x}_0)^{\frac{3}{4}}}{Fr^{\frac{5}{4}}} Re_b^{\frac{1}{4}}, \tag{6}$$

$$\tilde{t}_{IV} = \left(\frac{3\xi_{VP}}{10\xi_{IP}}\right)^{\frac{15}{7}} (\tilde{h}_0 \tilde{x}_0)^{\frac{4}{7}} Re_b^{\frac{3}{7}}, \tag{7}$$

$$Re_{cr} = \left(\frac{2\xi_{IP}}{3Fr}\right)^{12} \left(\frac{5Fr}{\xi_{VP}}\right)^5 \tilde{h}_0 \tilde{x}_0. \tag{8}$$

The time of transition from the slumping to inertial phase is a function of the initial non-dimensional lock length \tilde{x}_0 . It is often convenient to alter the non-dimensionalization of velocity and length scales, such that $\hat{u} = \tilde{u}_f/(\tilde{h}_0)^{\frac{1}{2}} = u_f/(g'h_0)^{\frac{1}{2}}$ and $\hat{t} = \tilde{t}(\tilde{h}_0)^{\frac{1}{2}}/\tilde{x}_0 = t(g'h_0)^{\frac{1}{2}}/x_0$, which causes the transition time to collapse down to $\hat{t}_{SI} = \left(2\xi_{IP}\tilde{h}_0^{\frac{1}{2}}/3Fr\right)^3$.¹⁸

A range of depth-resolving models have been developed to simulate the mechanics of dilute gravity currents. The models numerically solve the incompressible Navier–Stokes (NS) equations of mass and momentum conservation coupled, via the Boussinesq approximation, with an advection–diffusion equation for the scalar concentration field.¹⁹ As the dynamics of environmental gravity currents are substantially influenced by turbulent processes, such as turbulent mixing within the current and at the current–ambient interface, depth-resolving models are classified by the extent to which they resolve or model the turbulent length scales of the flow.

Numerical studies using direct numerical simulation (DNS), in which all turbulent length scales are resolved, have been conducted for lock-exchange gravity current flows with low-to-moderate Reynolds numbers.^{18,20–26} However, due to the high levels of grid refinement required for DNS simulations, the approach is extremely computationally expensive, which precludes the study of highly turbulent flows in large complex domains of the sort observed in the environment.

Reynolds-averaged Navier–Stokes (RANS) models, derived by time-averaging of the governing equations, have been applied to the simulation of dilute gravity currents with both fixed and deformable boundaries.^{27–32} Although RANS models are far less computationally expensive than DNS models, which has enabled the simulation of environmental scale flows, the inherent averaging of the governing equations reduces the accuracy with which they can capture the complex time-dependent turbulent flow features of gravity currents.

In large-eddy simulation (LES) models, the largest length scales are directly resolved, while the sub-grid scales of turbulent motion are modeled, usually using variants of the Smagorinsky model.³³ The grid resolution requirements for a well-resolved gravity current simulation have

been studied by Pelmard *et al.*³⁴ NS-LES models benefit from enhanced accuracy relative to RANS approaches as they directly capture the large-scale turbulent flow features, while offering a less computationally expensive alternative to DNS.^{34–39} However, the computational expense of conventional NS-LES models is still considerable, limiting the insights that can be gained into the dynamics of dilute gravity currents, as it becomes prohibitively expensive to extend the models to incorporate more of the full complexity of real-world environmental flows.

The lattice Boltzmann method (LBM) offers an alternative numerical framework to the aforementioned numerical methods, which all model fluid motion at the macroscopic scale, where the fluid and flow properties are continuous. The LB method differs fundamentally, as fluid motion is modeled at the mesoscopic scale, between macro and microscopic, where the fluid is described by a particle distribution function.⁴⁰ The evolution of the particle distribution function is governed by the Boltzmann equation, which is discretized to form an explicit numerical scheme. Guo *et al.*⁴¹ first demonstrated that an LBM formulation equivalent to the Navier–Stokes equations, using the Boussinesq approximation to couple the governing equations, could effectively simulate flows driven by density gradients.

LBM models have been formulated to solve the depth-averaged shallow water equations, to predict the current height and front velocity of gravity currents.⁴² However, there is very limited research on the application of LBM models to the simulation of gravity currents, where the LBM formulation is equivalent to the Navier–Stokes equations, and the Boussinesq approximation is applied. Ottolenghi *et al.*⁴³ published the first study of such a model, comparing the results of two and three-dimensional LBM large-eddy simulations (LBM–LES) of lock-exchange saline gravity currents against experimental data. Two-dimensional simulations were run for Reynolds numbers of $Re_b \in \{1000, 5000, 10\,000, 30\,000\}$, and three-dimensional simulations were run for $Re_b \in \{1000, 5000, 10\,000\}$. Ottolenghi *et al.*⁴³ made an initial comparison between the results of LBM simulations and experiments, demonstrating reasonable agreement with their experiments and theoretical results in the prediction of some key flow characteristics, such as the Froude number, entrainment of ambient fluid, and lobe-cleft development at the head. However, further validation is required, especially against DNS results, to determine whether the LBM framework can be used as an accurate numerical tool for the simulation of gravity currents.

The present study aims to address this open question and establish the LBM–LES method as an accurate alternative numerical framework for studying dilute gravity currents. Two LBM–LES codes, RAFSINE^{49,80} and VirtualFluids,^{78,79,81} are validated against a wide range of experimental data and high-resolution simulations. The key model performance tests, previously unaddressed in the literature, include the careful validation of LBM model predictions of flow phase transition against experimental data and high-resolution simulations, study of LBM–LES model accuracy in the near-wall region, and a comparison of the LBM–LES model accuracy to conventional NS-LES models. The accuracy and stability of an LBM model are influenced by the details of its formulation. The Ottolenghi *et al.*⁴³ LBM model uses a single relaxation time collision operator, which is the most widely used, but also the simplest of the available options. The LBM model implemented in VirtualFluids uses more advanced collision operators, creating potential for greater accuracy and stability in the simulations.⁴⁴

Additionally, the computational performance advantages of the LBM framework are also yet to be established. In the Ottolenghi *et al.*⁴³ study, the LBM model is implemented in an in-house code that utilizes OpenMP parallelization on CPU cores, resulting in simulation times ranging from 1 to 5 days on a six-core desktop machine. The authors acknowledge that this does not reflect the potential computational efficiency of the approach. LBM models are particularly well suited to implementation on massively parallel machines, such as graphic processing units (GPUs) as the numerical scheme only contains calculations with locally defined variables. This allows LBM algorithms to effectively utilize the architecture of the GPU. When simulations are run on central processing units (CPUs) with multi-core processors, the domain is divided between the various cores, which perform calculations in parallel and communicate when necessary. LBM model implementations on a GPU offer much greater potential for parallel fluid simulations than the CPU, as each node in the domain can be assigned to a different thread and stepped forward in time in parallel, resulting in orders of magnitude reductions in simulation times.⁴⁵ In the present study, simulations in RAFSINE and VirtualFluids are accelerated by exporting computations to a GPU. The computational performance of the LBM-GPU implementations is compared with conventional methods in the field to quantify the relative performance gains that are realized through the novel application of this framework.

The paper is structured as follows: the methods used to develop the LBM-LES models and the NS-DNS validation simulations are detailed in Sec. II; results and discussion regarding model accuracy and computational performance are presented in Sec. III; finally, conclusions are delivered in Sec. IV.

II. METHODS

A. Macroscopic governing equations

The macroscopic governing equations of a dilute saline gravity current flow are those of mass and momentum conservation for an incompressible flow coupled, via the Boussinesq approximation, with an advection–diffusion equation for the scalar concentration field. In the Boussinesq limit density $(\rho(\mathbf{x}, t))$ is a linear function of saline concentration and is defined in Eq. (9), where $\alpha = (\rho_s - \rho_a)/\rho_a$, ρ_s is solute density, and $\chi(\mathbf{x}, t)$ is solute concentration. Therefore, the macroscopic body force acting on the flow is \mathbf{G} , defined in Eq. (10), where $\mathbf{e}^g = (0, 0, -1)^T$ is the unit vector in the direction of gravitational acceleration. The constant term in \mathbf{G} is absorbed into the pressure term of the momentum equation as hydrostatic pressure, $\nabla P = \nabla(p_k(\mathbf{x}, t) - g\rho_a z)$, where p_k is kinematic pressure. Therefore, the flow is driven by the Boussinesq forcing term \mathbf{F}_B , Eq. (11),

$$\rho(\mathbf{x}, t) = \rho_a(1 + \alpha\chi(\mathbf{x}, t)), \quad (9)$$

$$\mathbf{G} = g\rho_a(1 + \alpha\chi(\mathbf{x}, t))\mathbf{e}^g, \quad (10)$$

$$\mathbf{F}_B = g\rho_a\alpha\chi(\mathbf{x}, t)\mathbf{e}^g. \quad (11)$$

Solute concentration in the ambient and dense fluids are set to zero ($\chi_a = 0$) and unity ($\chi_0 = 1$), respectively. The governing equations are non-dimensionalized using the characteristic length scale H , and velocity scale U_b , resulting in the non-dimensional incompressible mass and momentum conservation equations [Eqs. (12) and (13)], and an advection–diffusion equation for the scalar concentration field

$\tilde{\chi}(\mathbf{x}, t) = \chi(\mathbf{x}, t)/\chi_0$ [Eq. (14)]. Non-dimensional density is defined by the equation $\tilde{\rho}(\mathbf{x}, t) = (\rho(\mathbf{x}, t) - \rho_a)/(\rho_0 - \rho_a)$,

$$\nabla \cdot \tilde{\mathbf{u}} = 0, \quad (12)$$

$$\frac{\partial \tilde{\mathbf{u}}}{\partial t} + \tilde{\mathbf{u}} \cdot \tilde{\nabla} \tilde{\mathbf{u}} = -\tilde{\nabla} \tilde{P} + \frac{1}{Re_b} \tilde{\nabla}^2 \tilde{\mathbf{u}} + \tilde{\chi} \mathbf{e}^g, \quad (13)$$

$$\frac{\partial \tilde{\chi}}{\partial t} + \tilde{\mathbf{u}} \cdot \tilde{\nabla} \tilde{\chi} = \frac{1}{Re_b Sc} \nabla^2 \tilde{\chi}. \quad (14)$$

The governing equations contain two non-dimensional numbers, the buoyancy Reynolds number ($Re_b = U_b H/\nu$), and the Schmidt number ($Sc = \nu/D$), which is the ratio between the viscosity of the ambient fluid and the diffusivity of the scalar concentration field.

B. The lattice Boltzmann method framework

Conventional depth-resolving models directly discretize the macroscopic governing equations and solve them numerically. The lattice Boltzmann method models fluid motion at the mesoscopic scale, that is, between the micro and macroscopic scales. An overview of LBM theory is provided below, but readers are referred to Kruger *et al.*⁴⁴ for a rigorous derivation.

At the mesoscopic scale, distribution functions are the key variable and are used to represent the properties of a group of particles. The particle distribution function is an extension of volumetric mass density to include density in particle velocity space (ξ_x, ξ_y, ξ_z); hence, in three-dimensions, $f(\mathbf{x}, \xi, t)$ has the units presented in the following equation:

$$[f(\mathbf{x}, \xi, t)] = kg \cdot \frac{1}{m^3} \cdot \frac{1}{\left(\frac{m}{s}\right)^3} = \frac{kg s^3}{m^6}. \quad (15)$$

The particle distribution function is a function of the particle position vector (\mathbf{x}), particle velocity (ξ), and time (t). Therefore, the function returns the particle density within a specified velocity range at a given location and time. The total derivative of the particle distribution function produces the Boltzmann equation [Eq. (16)], which includes a source term $\Omega(f)$ to account for the collision and subsequent redistribution of particles. In the present study, the external body force term in the Boltzmann equation is the Boussinesq forcing term \mathbf{F}_B ,

$$Df(\mathbf{x}, \xi, t) = \partial_t f(\mathbf{x}, \xi, t) + \xi \cdot \nabla f(\mathbf{x}, \xi, t) + \mathbf{F}_B \cdot \partial_\xi f(\mathbf{x}, \xi, t) = \Omega(f). \quad (16)$$

The Boltzmann equation with forces is discretized to produce the lattice Boltzmann equation (LBE) with a momentum density source term (S_{ijk}) in Eq. (17). This is an expression for the unknown distribution function $f_{ijk}(\mathbf{x}, t)$, which is defined at the nodes of a lattice structure. The lattice is defined using the naming structure $DnQm$, where n indicates the number of spatial dimensions, and m is the number of discrete velocities. Three lattice structures are shown in Fig. 2, $D3Q6$, $D3Q19$, and $D3Q27$. Lattice nodes are connected by a set of discrete velocities (\mathbf{c}_{ijk}^{Qm}), where the indices i, j, k can take the values $\in \{1, 0, -1\}$, corresponding to each component of velocity in a Cartesian coordinate system. The lattice spacing is defined as Δx , and particles move between site locations in time Δt . The LBE is second-order accurate in both space and time⁴⁴

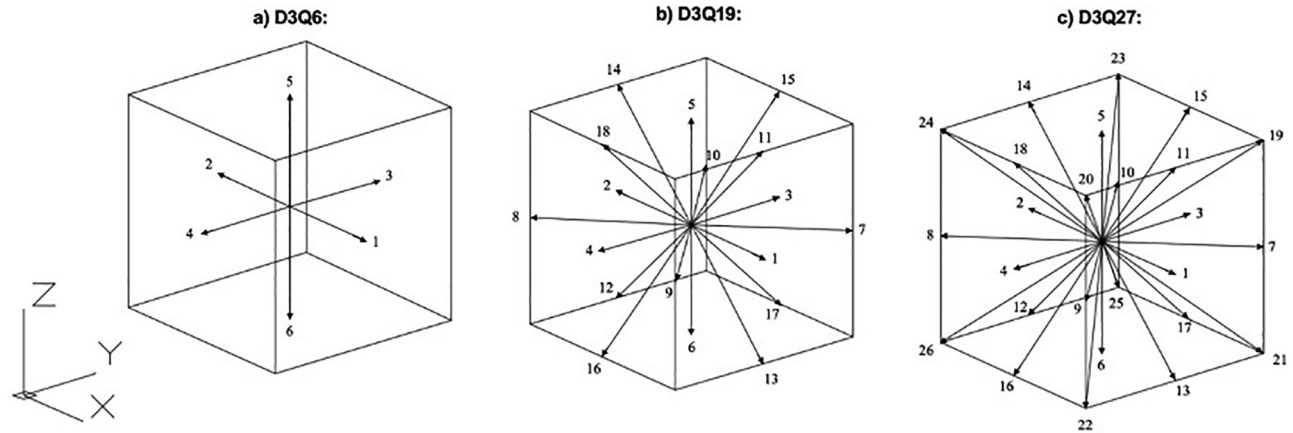


FIG. 2. Structure of (a) D3Q6, (b) D3Q19, and (c) D3Q27 lattices.

$$f_{ijk}(\mathbf{x} + \mathbf{c}_{ijk}^{Qm} \Delta t, t + \Delta t) = f_{ijk}(\mathbf{x}, t) + \Omega_{ijk}(f_{ijk}) + S_{ijk}. \quad (17)$$

The governing equations for macroscopic fluid flow, mass, and momentum conservation can be recovered from the Boltzmann equation using asymptotic analysis⁴⁶ or Taylor expansion.⁴⁷ The raw moments of the distribution function (f_{ijk}) are calculated using Eq. (18), where the order of the moment is determined by the sum of its indices $A + B + C$. Macroscopic density and momentum density are calculated from the zeroth- and first-order raw moments of f_{ijk} , respectively, as illustrated in the following equations:

$$m_{ABC} = \sum_{i,j,k} i^A j^B k^C f_{ijk}, \quad (18)$$

$$\rho = m_{000} = \sum_{i,j,k} f_{ijk}, \quad (19)$$

$$\rho \mathbf{u} = \rho(m_{100}, m_{010}, m_{001})$$

$$= \left(\sum_{i,j,k} i f_{ijk} + \frac{\Delta t}{2} F_B^x, \sum_{i,j,k} j f_{ijk} + \frac{\Delta t}{2} F_B^y, \sum_{i,j,k} k f_{ijk} + \frac{\Delta t}{2} F_B^z \right). \quad (20)$$

C. LBM implementations

An LBM gravity current model has been implemented in two codes, RAFSINE and VirtualFluids, which accelerate simulations by exporting computations to a GPU device. The broad structure of the LBM-GPU implementations is illustrated through a flow chart in Fig. 3. The flow chart emphasizes the transfer of data between the CPU and GPU and is broad enough to apply to both RAFSINE and VirtualFluids. Both packages are structured such that the pre-processing of the simulation, that is, the definition of simulation

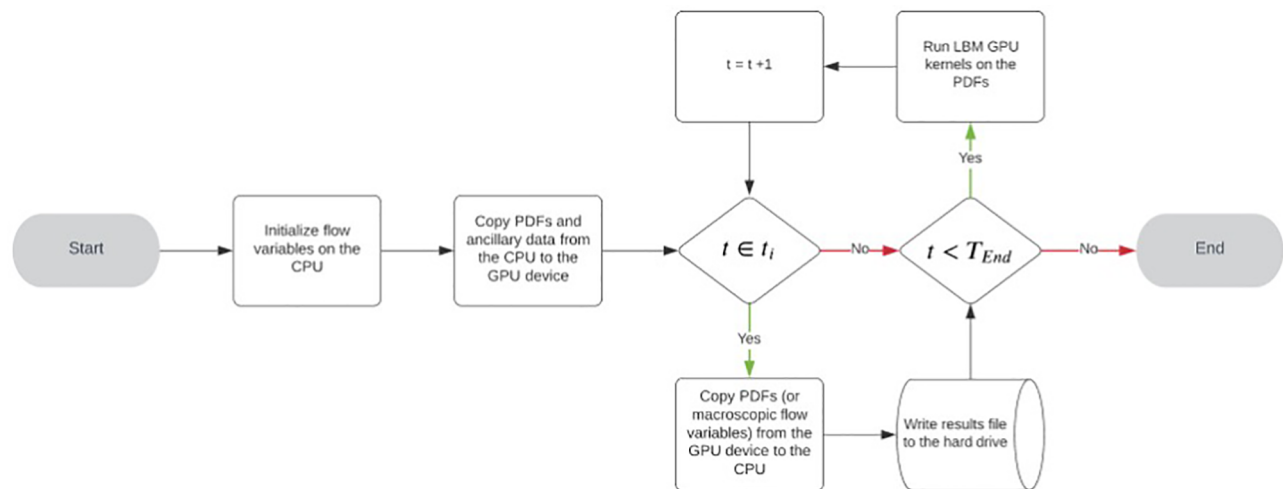


FIG. 3. Flowchart to outline the general structure of the LBM-GPU implementations in RAFSINE and VirtualFluids, with particular emphasis on the transfer of data between the CPU and GPU device.

parameters and geometry, is performed on the CPU, and then, data are exported to the GPU where the computations are accelerated. The two models utilize different collision operators (Ω_{ijk}), LES turbulence models, and GPU implementations, allowing for comparison of trade-offs in both accuracy and computational efficiency between the codes.

1. RAFSINE

RAFSINE was first developed by Delbosc⁴⁵ for the application of indoor airflow simulation. The version of the code applied in this study uses the BGK collision operator, which is also referred to as the single relaxation rate collision operator. The BGK approximation developed by Bhatnagar *et al.*⁴⁸ is widely used and is defined in Eq. (21), where f_{ijk}^{eq} is the equilibrium particle distribution function, Eq. (22). Bhatnagar *et al.*⁴⁸ model the collision operator as the relaxation of the particle distribution function toward a state of local thermodynamic equilibrium

$$\Omega_{ijk}(f) = \frac{1}{\tau} (f_{ijk}^{eq} - f_{ijk}). \quad (21)$$

The equilibrium is parametrized by the local velocity, density, and the speed of sound (related to the temperature), which is assumed to be constant in this lattice Boltzmann model. The Maxwellian equilibrium is simplified to a second order in velocity Taylor expansion, as shown in the following equation:

$$f_{ijk}^{eq}(\mathbf{x}, t) = w_{ijk}^{Q19} \rho \left(1 + \frac{\mathbf{u} \cdot \mathbf{c}_{ijk}^{Q19}}{c_s^2} + \frac{(\mathbf{u} \cdot \mathbf{c}_{ijk}^{Q19})^2}{2c_s^4} - \frac{\mathbf{u} \cdot \mathbf{u}}{2c_s^2} \right). \quad (22)$$

The velocity set \mathbf{c}_{ijk}^{Q19} and the constant set of weights w_{ijk}^{Q19} are defined in Eqs. (23) and (24) and correspond to the D3Q19 lattice, which is used to solve for the f_{ijk} distribution in RAFSINE. The D3Q19 lattice is shown in Fig. 2(b)

$$\mathbf{c}_{ijk \in \{-1, 0, 1\}}^{Q19} = \begin{pmatrix} i \\ j \\ k \end{pmatrix} = \begin{bmatrix} \begin{pmatrix} 0 \\ 0 \\ 0 \end{pmatrix}, \begin{pmatrix} 1 \\ 0 \\ 0 \end{pmatrix}, \begin{pmatrix} -1 \\ 0 \\ 0 \end{pmatrix}, \begin{pmatrix} 0 \\ 1 \\ 0 \end{pmatrix}, \begin{pmatrix} 0 \\ -1 \\ 0 \end{pmatrix}, \begin{pmatrix} 0 \\ 0 \\ 1 \end{pmatrix}, \begin{pmatrix} 0 \\ 0 \\ -1 \end{pmatrix}, \begin{pmatrix} 1 \\ 1 \\ 0 \end{pmatrix}, \begin{pmatrix} -1 \\ -1 \\ 0 \end{pmatrix}, \begin{pmatrix} 1 \\ -1 \\ 0 \end{pmatrix}, \\ \begin{pmatrix} -1 \\ 1 \\ 0 \end{pmatrix}, \begin{pmatrix} 1 \\ 0 \\ 1 \end{pmatrix}, \begin{pmatrix} -1 \\ 0 \\ 1 \end{pmatrix}, \begin{pmatrix} 1 \\ 0 \\ -1 \end{pmatrix}, \begin{pmatrix} -1 \\ 0 \\ -1 \end{pmatrix}, \begin{pmatrix} 0 \\ 1 \\ 1 \end{pmatrix}, \begin{pmatrix} 0 \\ -1 \\ -1 \end{pmatrix}, \begin{pmatrix} 0 \\ 1 \\ -1 \end{pmatrix}, \begin{pmatrix} 0 \\ -1 \\ 1 \end{pmatrix} \end{bmatrix}, \quad (23)$$

$$w_{ijk}^{Q19} \begin{cases} \frac{1}{3}, & \|\mathbf{c}_{ijk}^{Q19}\| = 0, \\ \frac{1}{18}, & \|\mathbf{c}_{ijk}^{Q19}\| = 1, \\ \frac{1}{36}, & \|\mathbf{c}_{ijk}^{Q19}\| = \sqrt{2}. \end{cases} \quad (24)$$

The macroscopic viscosity (ν) is derived from the characteristic relaxation time of the fluid (τ), as shown in Eq. (25), where $c_s = \sqrt{\Delta x^2 / (3\Delta t^2)}$ is the speed of sound in the lattice

$$\nu = c_s^2 \left(\tau - \frac{1}{2} \right) \frac{\Delta x^2}{\Delta t}. \quad (25)$$

The momentum density source term S_{ijk} is defined in the following equation:⁴⁴

$$S_{ijk} = \left(1 - \frac{\Delta t}{2\tau} \right) w_{ijk}^{Q19} \left(\frac{\mathbf{c}_{ijk}^{Q19}}{c_s^2} + \frac{(\mathbf{c}_{ijk}^{Q19} (\mathbf{c}_{ijk}^{Q19})^T - c_s^2 \boldsymbol{\delta}) \mathbf{u}}{c_s^4} \right) \cdot \mathbf{F}_B. \quad (26)$$

RAFSINE is capable of simulating density-driven flows by coupling two LBM equations, one for the conservation of mass and momentum in the fluid, and a second for the advection and diffusion of the concentration field (χ). The particle distribution function for the

concentration field is Φ_{ijk} , and its zeroth-order raw moment is the macroscopic concentration χ , as shown in Eq. (27). The equations are coupled via the Boussinesq approximation, as χ is used to update the local value of the forcing term \mathbf{F}_B at a given time step

$$\chi = \sum_{i,j,k} \Phi_{ijk}. \quad (27)$$

The LBM-BGK equation for the Φ_{ijk} distribution is presented in Eq. (28), where $\Phi_{ijk}^{eq}(\mathbf{x}, t)$ is the equilibrium distribution, defined in Eq. (29). The macroscopic diffusivity is determined by the relaxation time for the scalar field τ_Φ , as shown in Eq. (30)

$$\Phi_{ijk}(\mathbf{x} + \mathbf{c}_{ijk}^{Q6} \Delta t, t + \Delta t) = \Phi_{ijk}(\mathbf{x}, t) - \frac{1}{\tau_\Phi} (\Phi_{ijk}(\mathbf{x}, t) - \Phi_{ijk}^{eq}(\mathbf{x}, t)), \quad (28)$$

$$\Phi_{ijk}^{eq}(\mathbf{x}, t) = w_{ijk}^{Q6} \chi \left(1 + \frac{\mathbf{u} \cdot \mathbf{c}_{ijk}^{Q6}}{c_s^2} \right), \quad (29)$$

$$D = c_s^2 \left(\tau_\Phi - \frac{1}{2} \right) \frac{\Delta x^2}{\Delta t}. \quad (30)$$

A D3Q6 lattice [Fig. 2(a)] is used to solve for the Φ_{ijk} distribution in RAFSINE, in line with the formulation originally used by Delbosc *et al.*⁴⁹ The lattice has the velocity set \mathbf{c}_{ijk}^{Q6} , defined in Eq. (31), and a constant weight $w_{ijk}^{Q6} = 1/6$,

$$\begin{aligned} \mathbf{c}_{ijk \in \{-1,0,1\}}^{Q6} &= \begin{pmatrix} i \\ j \\ k \end{pmatrix} \\ &= \left[\begin{pmatrix} 1 \\ 0 \\ 0 \end{pmatrix}, \begin{pmatrix} -1 \\ 0 \\ 0 \end{pmatrix}, \begin{pmatrix} 0 \\ 1 \\ 0 \end{pmatrix}, \begin{pmatrix} 0 \\ -1 \\ 0 \end{pmatrix}, \begin{pmatrix} 0 \\ 0 \\ 1 \end{pmatrix}, \begin{pmatrix} 0 \\ 0 \\ -1 \end{pmatrix} \right]. \end{aligned} \quad (31)$$

The code utilizes a standard Smagorinsky turbulence model, which is an LES approach that models energy damping due to sub-grid turbulence through a local eddy viscosity (ν_T), such that $\nu = \nu_0 + \nu_T$, as given by Hou *et al.*⁵⁰

$$\nu_T = C_s \Delta^2 |\bar{\mathbf{S}}|, \quad (32)$$

$$\bar{\mathbf{S}} = \frac{1}{2} (\mathbf{V}\mathbf{u} + \mathbf{V}\mathbf{u}^T) = \sum_{i,j,k} \mathbf{c}_{ijk}^{Q19} \cdot \mathbf{c}_{ijk}^{Q19} (f_{ijk} - f_{ijk}^{eq}), \quad (33)$$

$$|\bar{\mathbf{S}}| = \frac{1}{6C_s \Delta^2} \left(\sqrt{\nu^2 + 18C_s^2 \Delta^2 \sqrt{\bar{\mathbf{S}}\bar{\mathbf{S}}} - \nu} \right). \quad (34)$$

The method assumes that small-scale turbulence is isotropic and is implemented using Eq. (32), where C_s is the Smagorinsky constant, Δ is the filter width, and $\bar{\mathbf{S}}$ is the local stress tensor, defined in Eq. (33). The magnitude of the local stress tensor is calculated from Eq. (34). The Smagorinsky constant is set to $C_s = 0.03$, according to the recommendations of Delbos.⁴⁵

The diffusivity of the scalar field is also influenced by the effects of sub-grid turbulence. In the Smagorinsky model, diffusivity is

calculated using Eq. (35), as determined by Liu *et al.*,⁵¹ where Sc_T is the turbulent Schmidt number, which is taken to be equal to C_s

$$D = c_s^2 \left(\left(\tau_\Phi + \frac{C_s \Delta^2 |\bar{\mathbf{S}}|}{Sc_T} \right) - \frac{1}{2} \right) \frac{\Delta x^2}{\Delta t}. \quad (35)$$

RAFSINE's LBM implementation contains several measures to maximize computational efficiency when running on GPUs. These include a number of adaptations to optimize the utilization of the GPU's memory bandwidth, such as eliminating redundant memory accesses, increasing data coalescence, and efficient reading/writing of distributions. Delbos *et al.*⁴⁹ demonstrated that the optimizations resulted in a computational performance just 6% below the maximum capacity of the available hardware. When validated against experimental data of thermal flow in a 32 m³ room, RAFSINE simulated the flow at 1.5 times real time on an NVIDIA Tesla C2070 GPU.

2. VirtualFluids

VirtualFluids was developed by the Institute for Computational Modeling in Civil Engineering (iRMB) at TU Braunschweig. VirtualFluids utilizes more advanced collision operators, namely, the factorized central moment method to solve for the advection-diffusion of the scalar field, and the cumulant collision operator to solve for the conservation of mass and momentum. A D3Q27 lattice, shown in Fig. 2(c), is used to solve for both the f_{ijk} and Φ_{ijk} distributions. The velocity set for the D3Q27 lattice is shown in the following equation:

$$\begin{aligned} \mathbf{c}_{ijk \in \{-1,0,1\}}^{Q27} &= \begin{pmatrix} i \\ j \\ k \end{pmatrix} = \left[\begin{pmatrix} 0 \\ 0 \\ 0 \end{pmatrix}, \begin{pmatrix} 1 \\ 0 \\ 0 \end{pmatrix}, \begin{pmatrix} -1 \\ 0 \\ 0 \end{pmatrix}, \begin{pmatrix} 0 \\ 1 \\ 0 \end{pmatrix}, \begin{pmatrix} 0 \\ -1 \\ 0 \end{pmatrix}, \begin{pmatrix} 0 \\ 0 \\ 1 \end{pmatrix}, \begin{pmatrix} 0 \\ 0 \\ -1 \end{pmatrix}, \begin{pmatrix} 1 \\ 1 \\ 0 \end{pmatrix}, \begin{pmatrix} -1 \\ -1 \\ 0 \end{pmatrix}, \begin{pmatrix} 1 \\ -1 \\ 0 \end{pmatrix}, \right. \\ &\quad \begin{pmatrix} -1 \\ 1 \\ 0 \end{pmatrix}, \begin{pmatrix} 1 \\ 0 \\ 1 \end{pmatrix}, \begin{pmatrix} -1 \\ 0 \\ 1 \end{pmatrix}, \begin{pmatrix} 1 \\ 0 \\ -1 \end{pmatrix}, \begin{pmatrix} -1 \\ 0 \\ -1 \end{pmatrix}, \begin{pmatrix} 0 \\ 1 \\ 1 \end{pmatrix}, \begin{pmatrix} 0 \\ -1 \\ 1 \end{pmatrix}, \begin{pmatrix} 0 \\ 1 \\ -1 \end{pmatrix}, \begin{pmatrix} 0 \\ -1 \\ -1 \end{pmatrix}, \\ &\quad \left. \begin{pmatrix} 1 \\ 1 \\ 1 \end{pmatrix}, \begin{pmatrix} 1 \\ -1 \\ 1 \end{pmatrix}, \begin{pmatrix} 1 \\ 1 \\ -1 \end{pmatrix}, \begin{pmatrix} 1 \\ -1 \\ -1 \end{pmatrix}, \begin{pmatrix} -1 \\ 1 \\ 1 \end{pmatrix}, \begin{pmatrix} -1 \\ -1 \\ 1 \end{pmatrix}, \begin{pmatrix} -1 \\ 1 \\ -1 \end{pmatrix}, \begin{pmatrix} -1 \\ -1 \\ -1 \end{pmatrix} \right]. \end{aligned} \quad (36)$$

The factorized central moment (FCM) method was applied to the advection-diffusion equation by Yang *et al.*⁵² While the BGK collision operator performs collisions in momentum space, relaxing distributions toward their equilibrium state, the factorized central moment method performs collisions in factorized central moment space. Moments of the discrete distribution function Φ_{ijk} can be obtained by first converting Φ_{ijk} into a continuous function using the Dirac delta function δ , as shown in the following equation:

$$\begin{aligned} \Phi(\boldsymbol{\xi}) &= \Phi(\xi_x + \xi_y + \xi_z) \\ &= \sum_{i,j,k} \Phi_{ijk} \delta(ic - \xi_x) \delta(jc - \xi_y) \delta(kc - \xi_z). \end{aligned} \quad (37)$$

The central moment generating function is then obtained by applying a bi-lateral Laplace transform to the function $\Phi(\mathbf{u} - \boldsymbol{\xi})$, as shown in Eq. (38). These are referred to as central moments, as $\Phi(\boldsymbol{\xi})$ has been

shifted into the frame of reference of the macroscopic fluid moving with velocity \mathbf{u} ,

$$\begin{aligned} F(\Xi) &:= \mathcal{L}\{\Phi(\mathbf{u} - \xi)\}(\Xi) \\ &= e^{-\Xi \cdot \mathbf{u}} \int_{-\infty}^{\infty} \Phi(\xi) e^{\Xi \cdot \xi} d\xi \\ &= e^{-\Xi \cdot \mathbf{u}} \sum_{i,j,k} \Phi_{ijk} \int_{-\infty}^{\infty} \delta(ic - \xi_x) \delta(jc - \xi_y) \delta(kc - \xi_z) e^{\Xi \cdot \xi} d\xi \\ &= \sum_{i,j,k} \Phi_{ijk} e^{\Xi(ic - \mathbf{u}) + Y(jc - v) + Z(kc - w)}. \end{aligned} \quad (38)$$

The moment generating function, $F(\Xi)$, is a function of the velocity-frequency variable $\Xi = \{\Xi, Y, Z\}$, and derivatives of $F(\Xi)$ produce non-orthogonal central moments of Φ_{ijk} of order $(n + r + s)$, as shown in the following equation:

$$\begin{aligned} \kappa_{nrs} &:= c^{-(n+r+s)} \left. \frac{\partial^n \partial^r \partial^s}{\partial \Xi^n \partial Y^r \partial Z^s} F(\Xi) \right|_{\Xi=0} \\ &= \sum_{i,j,k} (i - u)^n (j - v)^r (k - w)^s \Phi_{ijk}. \end{aligned} \quad (39)$$

Statistical independence of the central moments can be achieved by factorizing them.⁵³ The factorized central moments are calculated using Eqs. (40)–(49), where brackets are used to denote permutations of the indices⁵²

$$M_{000} = \kappa_{000} = \chi, \quad (40)$$

$$M_{(100)} = \kappa_{(100)}, \quad (41)$$

$$M_{(110)} = \kappa_{(110)}, \quad (42)$$

$$M_{111} = \kappa_{111}, \quad (43)$$

$$M_{(200)} = \kappa_{(200)} - \frac{1}{3} \kappa_{000}, \quad (44)$$

$$M_{(210)} = \kappa_{(210)} - \frac{1}{3} \kappa_{(010)}, \quad (45)$$

$$M_{(220)} = \kappa_{(220)} - \frac{1}{3} \kappa_{000}, \quad (46)$$

$$M_{(221)} = \kappa_{(221)} - \frac{1}{9} \kappa_{(001)}, \quad (47)$$

$$M_{(211)} = \kappa_{(211)} - \frac{1}{3} \kappa_{(011)}, \quad (48)$$

$$M_{222} = \kappa_{222} - \frac{1}{27} \kappa_{000}. \quad (49)$$

Collision is then performed in moment space, where moments M_{nrs} are relaxed at the frequency ω_{nrs} , toward their equilibria, which for factorized central moments is set to zero. The postcollision moments M_{nrs}^* are calculated using the following equation:

$$M_{nrs}^* = (1 - \omega_{nrs}) M_{nrs}. \quad (50)$$

When applied to the advection–diffusion equation, the only conserved moment is $M_{000} = \chi$. Diffusivity is calculated using the relaxation frequency of $\kappa_{(100)}$, as shown in the following equation:

$$D = \frac{1}{3} \left(\frac{1}{\omega_{100}} - \frac{1}{2} \right) \frac{\Delta x^2}{\Delta t}. \quad (51)$$

The VirtualFluids code solves the incompressible LBM equation in which fluid density is decomposed into its mean ($\bar{\rho}$) and fluctuating ($\delta\rho$) components, as shown in Eq. (52). The $\delta\rho$ component is calculated by the zeroth raw moment of the distribution f_{ijk} [Eq. (53)], and the $\bar{\rho} = 1$ in lattice units

$$\rho = \bar{\rho} + \delta\rho, \quad (52)$$

$$\delta\rho = m_{000} = \sum_{i,j,k} f_{ijk}. \quad (53)$$

The cumulant collision operator is used to solve for mass and momentum conservation in the fluid.⁵⁴ The cumulant operator performs collisions in cumulant space, where cumulants are statistically independent observable quantities of the momentum distribution f_{ijk} . They are calculated from the series expansion of the logarithm of the moment generating function $\mathcal{L}\{f(-\xi)\}(\Xi)$, as shown in the following equation:

$$C_{nrs} := c^{-(n+r+s)} \left. \frac{\partial^n \partial^r \partial^s}{\partial \Xi^n \partial Y^r \partial Z^s} \ln(\mathcal{L}\{f(-\xi)\}(\Xi)) \right|_{\Xi=0}. \quad (54)$$

The postcollision cumulants C_{nrs}^* are calculated using Eq. (55), where C_{nrs}^{eq} is the equilibrium cumulant

$$C_{nrs}^* = (1 - \omega_{nrs}) C_{nrs} + \omega_{nrs} C_{nrs}^{eq}. \quad (55)$$

The process for performing efficient transformations between momentum space and cumulant space is detailed by Geier *et al.*⁵⁵ As the cumulant collision operator is applied to the conservation of mass and momentum, the zeroth- and first-order cumulants are conserved, which relate to density and velocity as shown in the following equations:

$$\rho = C_{000}, \quad (56)$$

$$\mathbf{u} = (u, v, w) = (C_{100}, C_{010}, C_{001}). \quad (57)$$

Viscosity is calculated using the relaxation rate of the second-order cumulants, the following equation:

$$\nu = \frac{1}{3} \left(\frac{1}{\omega_{110}} - \frac{1}{2} \right) \frac{\Delta x^2}{\Delta t}. \quad (58)$$

A cumulant collision operator is deemed to be more accurate than the BGK collision operator due to the incorporation of higher order velocity terms in the equilibrium and its Galilean invariant viscosity.⁵⁴ The current study applies the parameterized cumulant method of Geier *et al.*⁵⁵ The relaxation rates of the third-order cumulants are chosen to eliminate the leading order error in diffusion such that the handling of viscosity becomes essentially fourth-order accurate.

VirtualFluids does not incorporate a sub-grid eddy viscosity turbulence model, which would destroy the advantage of the fourth-order accuracy. To stabilize the method for resolutions not reaching DNS quality, it is sufficient to add a limiter on the relaxation of the third-order cumulants. Compared to adding an explicit sub-grid model, the stabilized parametrized cumulant method has been shown to require half the resolution to obtain the same enstrophy production.⁵⁶ The method was also successful in accurately predicting the drag crisis behind a sphere,⁵⁷ simulating flows with Reynolds numbers ranging from 200 to 10^5 . The approach taken by the cumulant method toward turbulence is to provide the highest possible accuracy even at low resolution, while non-resolved scales are naturally cut off. Adding a

TABLE I. Saline current LBM-LES simulation parameters.

Case No.	Re_b	L_3/x_0	L_1	L_2	N_{L_3}	N_{nodes} (10^6)	Data type	Data source
1	895	1	25	1.5	100	37.5	DNS	Cantero <i>et al.</i> ¹⁸
2	1 000	1	15	1	100	15	DNS; Exp	Nek5000; Ottolenghi <i>et al.</i> ⁴³
3	3 450	1	25	1.5	100	37.5	DNS	Cantero <i>et al.</i> ¹⁸
4	5 000	1	15	1	100	15	DNS; Exp	Nek5000; Ottolenghi <i>et al.</i> ⁴³
5	8 950	1	25	1.5	100	37.5	DNS	Cantero <i>et al.</i> ¹⁸
6	10 000	1	15	1	100	15	Exp	Ottolenghi <i>et al.</i> ⁴³
7	15 000	1	25	1.5	104	42.2	DNS	Cantero <i>et al.</i> ²¹
8	30 000	1	15	1	140	41.2	Exp	Ottolenghi <i>et al.</i> ⁴³

sub-grid model to the parameterized cumulant method has no known advantages and typically leads to inferior results.⁵⁶

VirtualFluids has been optimized to run on GPUs, using indirect addressing to facilitate simulation in complex geometries, and the Esoteric Twist data structure to minimize memory overhead and traffic on the GPU.⁵⁸

Previous studies in VirtualFluids have considered passive scalar transport in which the cumulant and FCM kernels are one-way coupled, so buoyancy forces do not drive the flow.^{52,59} In the present study, two-way coupling has been implemented to allow the simulation of a buoyancy driven gravity current flow.

D. Nek5000 direct numerical simulations

Direct numerical simulations are run in the high-order solver Nek5000 to provide high-resolution simulation results against which to benchmark the LBM-LES codes, in addition to that already available in literature. Nek5000-v19.0⁸² is a CFD solver developed by Argonne National Laboratory⁶⁰ based on the spectral-element method (SEM).⁶¹ The approach discretizes the computational domain into E elements, each containing an Nth-order polynomial discretization. In the present study, seventh-order polynomials were used for optimal accuracy and performance.⁶⁰ The non-dimensional governing equations outlined in Sec. II A were solved in Nek5000 using second-order backward differential formula (BDF) and operator-integration factor

scheme (OIFS) extrapolation, which allows for a target Courant number of 2–5 while maintaining stability and accuracy.⁶² The residual tolerance for pressure was set to 10^{-9} , while the tolerances for fluid velocity and concentration were set to 10^{-10} .

E. Lock-exchange saline gravity current model

The full list of test cases is presented in Table I, where the channel dimensions ($L_1, L_2, L_3 = H$) are defined in Fig. 4. N_{L_3} is the number of nodes used to resolve the channel depth H , and N_{nodes} is the total number of mesh points in the computational domain.

The LBM-LES models are validated against the DNS results published by Cantero *et al.*,^{18,21} where simulations were run with buoyancy Reynolds numbers ranging from $Re_b \in [895, 15\,000]$. As DNS becomes prohibitively expensive at high Reynolds numbers, it was also necessary to validate against the experimental results of Ottolenghi *et al.*,⁴³ where experiments were conducted for Reynolds numbers ranging from $Re_b \in [1000, 30\,000]$. To achieve a more robust validation, DNS simulations were run in Nek5000 for cases 2 and 4 in Table I.

The geometry and boundary conditions used in cases $\in \{2, 4, 6, 8\}$, outlined in Fig. 4(a), were selected to model the experimental conditions of Ottolenghi *et al.*⁴³ A no-slip boundary condition for the velocity field and a no-flux boundary condition for the concentration field is applied on the upper and lower boundaries, end walls, and spanwise walls. The initial velocity was zero throughout the

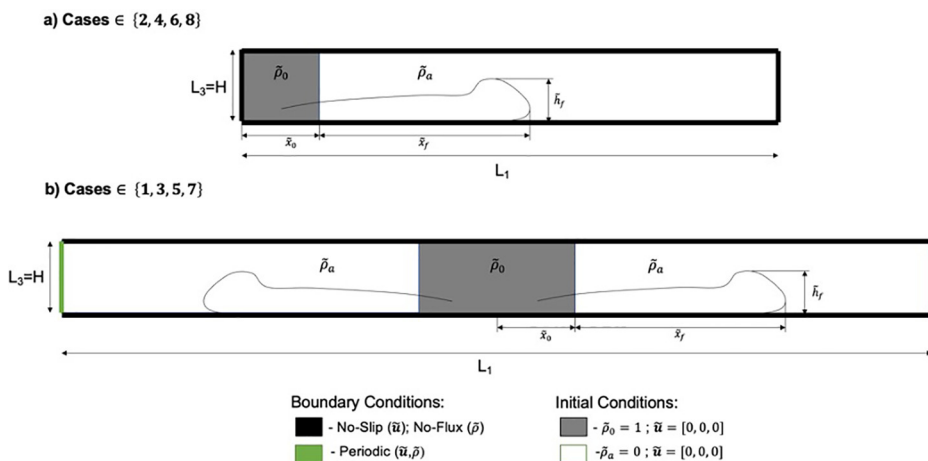


FIG. 4. Initial and boundary conditions of saline gravity current simulations of (a) cases $\in \{2, 4, 6, 8\}$ and (b) cases $\in \{1, 3, 5, 7\}$.

domain, while the concentration was set to $\tilde{\chi} = 1$ within the lock, and $\tilde{\chi} = 0$ elsewhere.

The geometry and boundary conditions applied in cases $\in \{1, 3, 5, 7\}$, outlined in Fig. 4(b), are in alignment with those used by Cantero *et al.*^{18,21} A no-slip boundary condition for the velocity field and a no-flux boundary condition for the concentration field is applied on the upper and lower boundaries, while the end and spanwise wall are periodic, thereby producing a periodic array of gravity currents. The initial velocity was zero throughout the domain, while the concentration was set to $\tilde{\chi} = 1$ within the lock, and $\tilde{\chi} = 0$ elsewhere. However, due to the periodic spanwise boundaries, a small random perturbation was applied at the surface of the gate to initiate a break-down into fully three-dimensional flow.

No-slip and no-flux boundary conditions in the LBM–LES models were implemented using halfway bounce-back boundary conditions, as is conventional in the field.^{43,44,52,63} Simulations in RAFSINE and VirtualFluids were run on a regularly spaced grid of nodes with a non-dimensional grid spacing of $\Delta\tilde{x} = H/N_{L_3}$. The Nek5000 simulations for cases 2 and 4 were run on grids of resolution $1600 \times 120 \times 120$ and $2000 \times 184 \times 184$, respectively.

The LBM simulations are run in lattice units (LU), where conversion between LU and non-dimensional units is achieved through the length scale $\Delta\tilde{x}$, and timescale $\Delta\tilde{t}$. Appropriate Reynolds number scaling in the LBM models is achieved by adjusting viscosity in lattice units. The characteristic velocity in lattice Boltzmann units is fixed at a value of $U_b \text{LU} = 0.03$, that is, $\tilde{U}_b = U_b \text{LU} \Delta\tilde{x} / \Delta\tilde{t} = 0.03 \Delta\tilde{x} / \Delta\tilde{t}$. This was motivated by the recommendations of Krüger *et al.*⁴⁴ on maintaining accuracy and stability. As the value of the non-dimensional velocity scale is $\tilde{U}_b = 1$, the non-dimensional time step for a simulation is given by $\Delta\tilde{t} = 0.03 / N_{L_3}$. The reduced gravity for a simulation can then be calculated as $\tilde{g}' = g' \text{LU} \Delta\tilde{x} / \Delta\tilde{t}^2 = \frac{0.03^2}{N_{L_3}^2} \Delta\tilde{x} / \Delta\tilde{t}^2$. As the characteristic length scale $H = N_{L_3} \Delta\tilde{x}$, viscosity is calculated as $\tilde{\nu} = \nu \text{LU} \Delta\tilde{x}^2 / \Delta\tilde{t} = \frac{N_{L_3} 0.03}{Re_b} \Delta\tilde{x}^2 / \Delta\tilde{t}$, for a given Reynolds number. In this study, the Schmidt number is set to 1; therefore, $\tilde{\nu} = \tilde{D}$ in all simulations.

III. RESULTS AND DISCUSSION

In this section, the LBM–LES models are assessed based on their ability to predict the following key characteristics of a lock-exchange gravity current; front location and velocity within the slumping phase, transition to the inertial and/or viscous phases, the development of the correct qualitative turbulent flow features in the head and body, and wall shear stress on the lower boundary. Additionally, the computational expense of the RAFSINE and VirtualFluids codes is compared to recently developed NS-LES models of equivalent accuracy.

A. Slumping phase

As outlined in Sec. I, the slumping phase is characterized by a period of constant front velocity in which $\tilde{x}_f \propto \tilde{t}$. In the numerical simulations, the span-averaged location of the current head, \tilde{x}_f , was determined by calculating the spanwise average of the density field, $\bar{\rho}(\tilde{x}, \tilde{z}) = \frac{1}{L_2} \int_0^{L_2} \tilde{\rho} d\tilde{y}$, and then searching from $\tilde{x} = L_1$ to $\tilde{x} = 0$ for the first node with a density below the interface threshold of $\tilde{\rho} = 0.02$. This threshold has been used previously by Ottolenghi *et al.*,⁴³ and it

was easily verified that the computed front location was insensitive to variations in the threshold.

Plots of current front location against time are presented for each case in Fig. 5, except for case 7 as validation data were not readily available for a direct comparison in the Cantero *et al.*²¹ publication. The $\tilde{x}_f \propto \tilde{t}$ curve is also plotted for reference. In each case, both RAFSINE and VirtualFluids accurately capture the slumping phase, predicting a constant gradient in \tilde{x}_f until $\tilde{t} \approx 10$. Additionally, within the slumping phase, the computed front locations from both LBM–LES codes are in close agreement with the DNS results of Nek5000 and the Cantero *et al.*¹⁸ study. In cases 6 and 8, where the codes are validated against experimental results, good agreement is observed with the experiments and LBM simulations of Ottolenghi *et al.*⁴³

The accuracy of the slumping phase simulation can be verified more quantitatively through the Froude number, defined in Eq. (59) as the constant non-dimensional front velocity within the slumping phase. It is evaluated within the time range of $2.5 \leq \tilde{t} \leq 10$,

$$Fr = \left. \frac{d\tilde{x}_f}{dt} \right|_{2.5 \leq \tilde{t} \leq 10} \quad (59)$$

The percentage error in the front velocity predictions of RAFSINE and VirtualFluids are presented in Table II, where error is calculated relative to the results in the validation sources listed in Table I, and is reported to two decimal places. All errors are less than 5%, demonstrating close quantitative agreement with the reference data.

The accuracy of the Froude number predictions of both codes is equal to that of conventional NS-LES models. Ooi *et al.*⁶⁴ reported Froude number predictions within ± 0.01 of the reference data in their validation of a finite-volume LES code against the Hacker *et al.*⁶⁵ lock-exchange experimental results, for Reynolds numbers of $Re_b \in \{30\,980, 47\,750, 87\,750\}$.

More recently, an LES study conducted by Pelmard *et al.*,³⁸ also using a finite-volume method code, observed an error of approximately 4.17%, when validating the results of a $Re_b = 60\,000$ simulation against the experiments of Keulegan.⁶⁶

In cases 4 and 6, $Re_b \in \{5000, 10\,000\}$, both RAFSINE and VirtualFluids demonstrate similar accuracy to the 3D LBM model of Ottolenghi *et al.*,⁴³ displaying errors of less than 3%. However, in case 2, $Re_b = 1000$, both RAFSINE and VirtualFluids predict the same Froude number as the DNS result, while the Ottolenghi *et al.*⁴³ model has an error of 5.4%. Additionally, it is clear from Fig. 5(b) that although there is close agreement in the front location predictions of RAFSINE/VirtualFluids and the Nek5000 result, there are discrepancies between the front location predicted by the Nek5000 DNS simulation and the numerical and experimental results of Ottolenghi *et al.*⁴³ These discrepancies are better understood through analysis of the front velocity and transition to the inertial and/or viscous phases of the flow, which is presented in Sec. III A.

In addition to achieving close quantitative agreement with the reference DNS and experimental results, visualizations of the density fields in the LBM–LES simulations demonstrates that the models capture the qualitative features of a slumping lock-exchange gravity current flow. Iso-contours of density $\tilde{\rho} = 0.02$, the chosen interface between the current and ambient, are presented in Fig. 6 for cases with $Re_b \in \{1000, 5000, 10\,000, 30\,000\}$ at $\tilde{t} = 10$, to illustrate the development of turbulent flow features in the LBM–LES simulations across a range of Reynolds numbers. The iso-contours are plotted in a

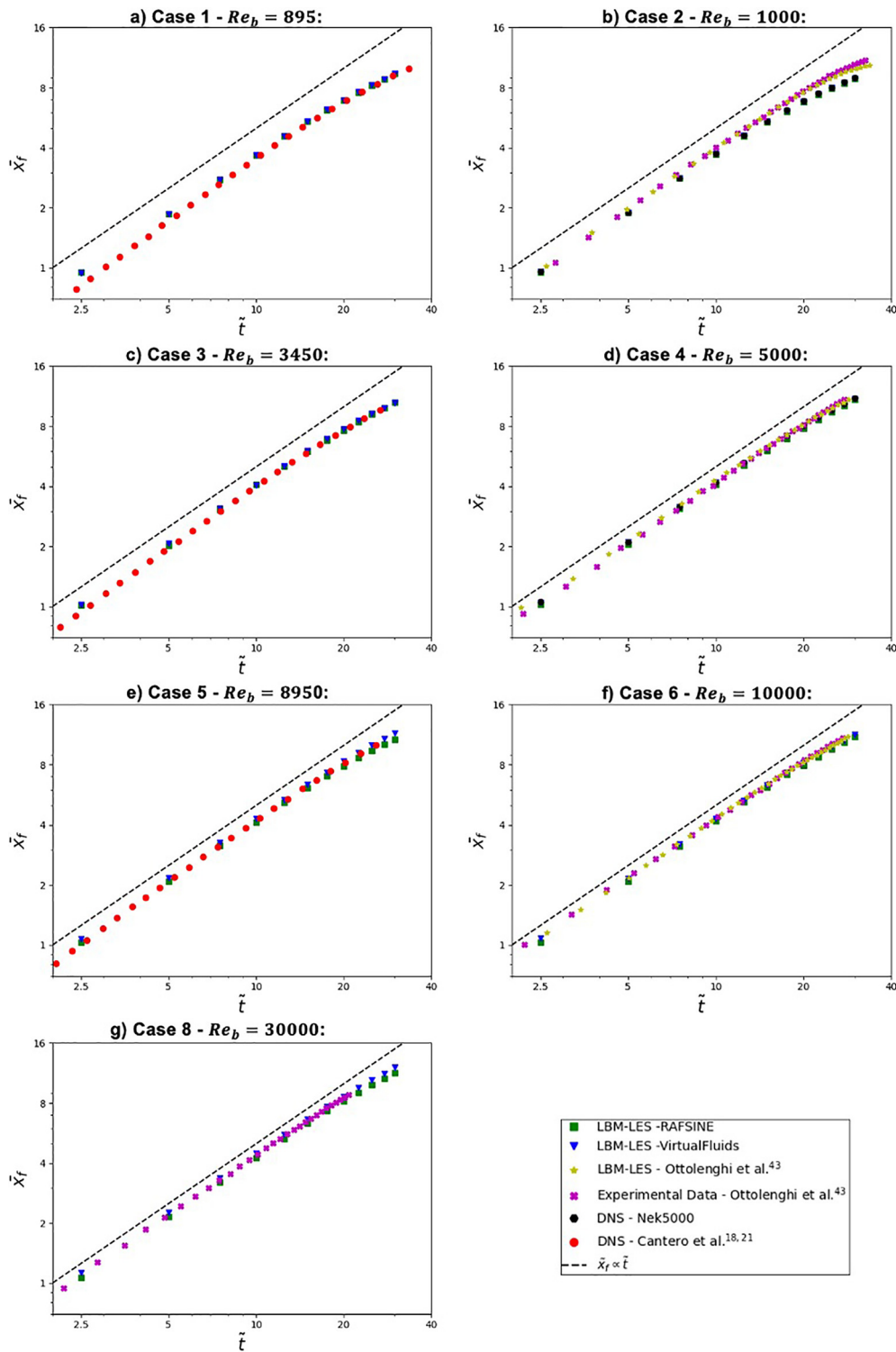


FIG. 5. Validation of the front location predictions of RAFSINE and VirtualFluids for (a) case 1, (b) case 2, (c) case 3, (d) case 4, (e) case 5, (f) case 6, and (g) case 8. Results are validated against the DNS results from Nek5000 and those of Cantero *et al.*¹⁸ as well as the experimental and numerical results of Ottolenghi *et al.*⁴³ In (h), the front location prediction from the $Re_b = 30\,000$, Pelmard *et al.*³⁴ NS-LES simulation is also plotted.

19 February 2024 14:18:55

TABLE II. Validation of the Froude number predictions of RAFSINE and VirtualFluids against DNS results and experimental data.

Case No.	Re_b	DNS/experimental result		VirtualFluids		RAFSINE	
		Data source	Fr	Fr	Error (%)	Fr	Error (%)
1	895	DNS—Cantero <i>et al.</i> ¹⁸	0.36	0.37	2.70	0.36	0.00
2	1 000	DNS—Nek5000, present study	0.37	0.37	0.00	0.37	0.00
3	3 450	DNS—Cantero <i>et al.</i> ¹⁸	0.41	0.41	0.00	0.40	2.44
4	5 000	DNS—Nek5000, present study	0.42	0.42	0.00	0.41	2.38
5	8 950	DNS—Cantero <i>et al.</i> ¹⁸	0.42	0.43	2.38	0.41	2.38
6	10 000	Exp.—Ottolenghi <i>et al.</i> ⁴³	0.42	0.42	0.00	0.42	0.00
7	15 000	DNS—Cantero <i>et al.</i> ²¹	0.42	0.44	4.65	0.42	0.00
8	30 000	Exp.—Ottolenghi <i>et al.</i> ⁴³	0.44	0.45	2.27	0.43	2.27

sub-region of the full computational domain, ranging from $\tilde{x} \in [0, 6]$, $\tilde{y} \in [0, 1]$, and $\tilde{z} \in [0, 1]$.

Density iso-contours from the RAFSINE, VirtualFluids, and Nek5000 DNS simulations of case 2 and 4, $Re_b = 1000$ and 5000 , are presented in Figs. 6(a) and 6(b), respectively. The results show that in both cases the structure of the current interface in the LBM–LES models shows close agreement with the DNS simulation. The iso-contours of case 2, $Re_b = 1000$, do not exhibit any significant turbulent flow features. The interface between the dense current and ambient is relatively smooth and flat in the body, and the head advances as a unified front. The current interface in case 4, $Re_b = 5000$, exhibits clear turbulent flow features, in agreement with observations from previous DNS simulations at similar Reynolds numbers.²⁰ Lobe and cleft structures are visible at the lower boundary of the current front, due to instabilities at the head. Additionally, a region of turbulent mixing is evident at the current–ambient interface in the body due to the Kelvin–Helmholtz instability. It is expected that subtle differences may be observed between the interface structure at a single time (e.g., $\tilde{t} = 10$), as we are monitoring a turbulent time-dependent flow. Given this caveat, both RAFSINE and VirtualFluids show good agreement with the DNS result.

The density iso-contours produced by the RAFSINE and VirtualFluids simulations of cases 6 and 8 are presented in Figs. 6(c) and 6(d), respectively. Unfortunately, DNS iso-contours are not available for direct comparison. Figures 6(c) and 6(d) show that, as anticipated, with the increasing Reynolds number there is an intensification of the turbulent flow features observed in case 4, Fig. 6(b). While at low Reynolds numbers, there were negligible differences between the current–ambient interface in the RAFSINE and VirtualFluids simulations, significant differences are visible at higher Reynolds numbers.

The interface in the VirtualFluids simulation exhibits more small-scale folds and structures relative to the RAFSINE result, a contrast that is most clearly observed in Fig. 6(d). Additionally, it is anticipated that with increasing Reynolds number, the size of lobes will decrease, and their number will increase.^{18,20,67} This trend is observed in the results of both LBM–LES models but appears to happen more rapidly in VirtualFluids. This is likely the result of differences in turbulence production due to shear on the lower boundary in both models. Validation of shear stress on the lower boundary, detailed in Sec. III B, indicates that shear stress is significantly underpredicted in RAFSINE at high Reynolds numbers. As shear stress on the lower boundary is a

key mechanism of turbulence generation, an underprediction of shear stress would suppress the development of turbulent flow features. Despite these observable differences in the current–ambient interface, both LBM–LES models produce equivalent accuracy in Froude number predictions across the high Reynolds number cases, see Table I.

A. Transition to inertial and viscous phases

The transition between the various phases is most clearly observed through the spanwise averaged front velocity of the current $\bar{u}_f = \frac{dx_f}{dt}$. Plots of spanwise averaged front velocity against time are presented in Fig. 7 for cases with Reynolds numbers of $Re_b \in \{1000, 5000, 8950, 10\,000, 15\,000, 30\,000\}$. In addition to the results from the validation data sources listed in Table I, results are plotted from other lock-exchange experiments in the literature with relatively similar Reynolds numbers. The scaling law predictions, using the revised empirical constants determined by Cantero *et al.*,¹⁸ are also plotted for each case.

As outlined in Sec. I, following the slumping phase the flow transitions into the inertial phase if the Reynolds number exceeds the critical value defined in Eq. (8) in which case the inertial phase transition time (\tilde{t}_{SI}) is smaller than the viscous phase transition time (\tilde{t}_{SV}). It was therefore anticipated that the inertial phase would only develop in cases 3–8.

The results presented in Fig. 7 permit comparison of the LBM–LES front velocity predictions against the scaling laws, experimental data, and DNS results. Each offers a source of validation but has its own limitations. As outlined in Sec. I, the scaling laws are derived directly from the governing equations but contain empirical constants that are fit by collating experimental and numerical results. Therefore, although the asymptotic behavior of the front velocity with time should match the scaling law, there may be small errors in the quantitative prediction of front velocity. Additionally, as the scaling laws were parameterized using some of the empirical data plotted in Fig. 7, the scaling laws and individual experimental results are not wholly independent sources of validation.

The experimental data are a record of a real-world lock-exchange gravity current flow but is itself subject to error. Errors may accumulate from the natural variability in the system, in the measurement of material properties, in the measurement of concentration and velocity fields, and in the image post-processing required to analyze the results.

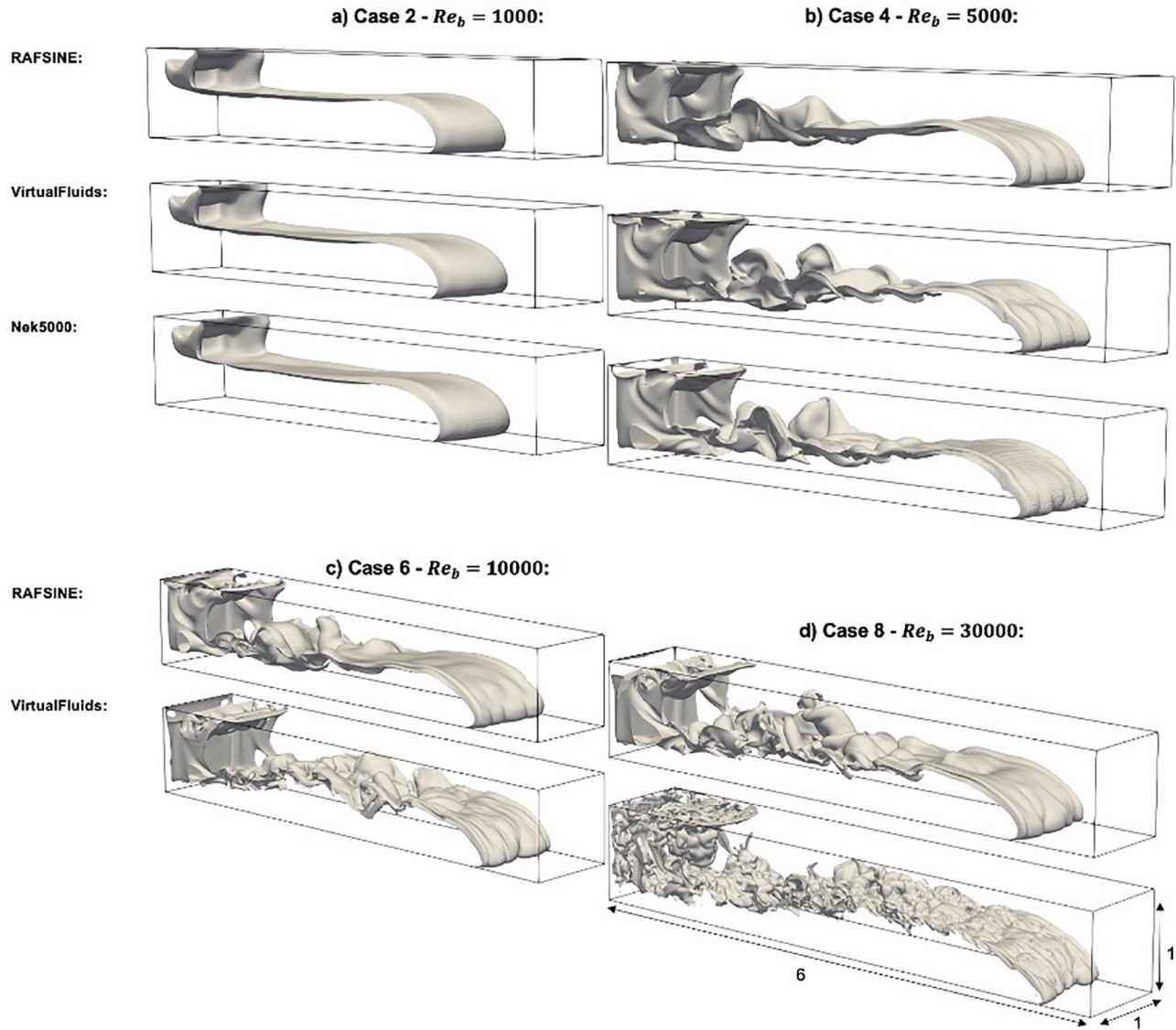


FIG. 6. Iso-contours of density $\bar{\rho} = 0.02$ at $\bar{t} = 10$ in the Nek5000, VirtualFluids, and RAFSINE simulations. (a) case 2, $Re_b = 1000$; (b) case 4, $Re_b = 5000$; (c) case 6, $Re_b = 10000$; (d) case 8, $Re_b = 30000$.

These limitations are revealed through the data spread when comparing experimental data sets from multiple sources with the same input parameters, as can be observed when comparing the spread of experimental data plotted in Figs. 7(a), 7(e), and 7(f).

DNS results provide the best source of validation data for theoretical and numerical models as the Navier–Stokes and advection–diffusion equations are solved directly across all length scales. Therefore, a DNS result forms an upper limit on simulation accuracy. However, a DNS or other numerical simulation result is still the solution of an idealized mathematical formulation of the problem, which may not map onto the physical reality and pragmatic constraints of a lock-exchange experiment.

Simulations commonly assume perfectly smooth walls, while experiments will have some degree of microscale roughness which

impacts drag.⁶⁸ Additionally, the simulations assume instantaneous removal of the gate, while in reality subtle inconsistencies in the speed of gate removal may have a significant impact on the resulting current dynamics.^{69,70} Nevertheless, collectively the scaling laws, experimental data, and DNS results provide a framework for assessing the accuracy of LBM–LES models.

From the relatively low Reynolds number cases ($Re_b \leq 5000$), the front velocity results for cases 2 and 4 have been selected [Figs. 7(a) and 7(b)], as they allow for comparisons between the results of the Nek5000 DNS simulations, the predictions of RAFSINE and VirtualFluids, and the experimental and numerical results of Ottolenghi *et al.*⁴³ In case 5, where $Re_b = 5000$ and $Fr = 0.42$, transition to the slumping phase occurs at $\bar{t} \approx 11$ in the Nek5000 DNS model. The scaling laws predict

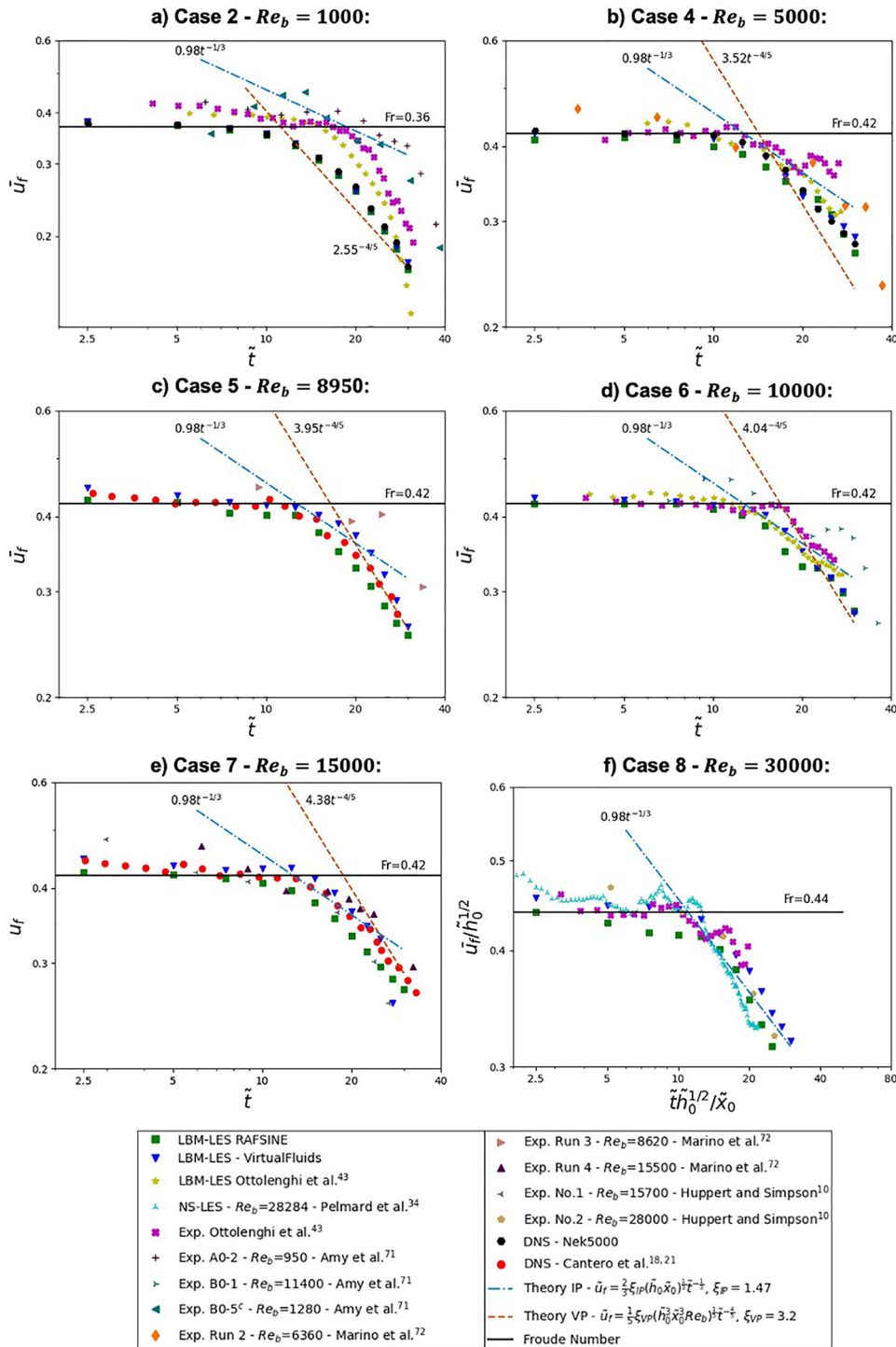


FIG. 7. Validation of front velocity predictions of the LBM-LES models for (a) case 2, (b) case 4, (c) case 5, (d) case 6, (e) case 7, and (f) case 8. Results are validated against the DNS results from Nek5000 and those of Cantero *et al.*,^{18,21} as well as comparison to the experimental and numerical result of Ottolenghi *et al.*⁴³ In (h), the front location prediction from the $Re_b \approx 30000$ Pelmaerd *et al.*³⁴ NS-LES simulation is also plotted. Front velocity within the inertial (IP) is compared with the theoretical scaling laws.^{10,13-15} Within the viscous phase (VP), front velocity is compared to the theoretical scaling laws established by Huppert.¹⁷ The scaling laws are calculated using $\xi_p = 1.47$ and $\xi_{p,HP} = 3.2$, which are the revised values as determined by Cantero *et al.*¹⁸

19 February 2024 14:18:55

that transition to the inertial phase should happen at $\tilde{t}_{SI} = 12.7$, which is in reasonable agreement with the DNS result.

The transition time predicted by RAFSINE and VirtualFluids, and the experimental and numerical results of Ottolenghi *et al.*⁴³ are in good

agreement with the DNS result. Within the inertial phase, front velocity in the DNS and LBM-LES simulations scale according to the $\bar{u}_f \propto \tilde{t}^{-1/3}$ law. The scaling laws predict a short inertial phase with the transition to the viscous phase occurring at $\tilde{t}_{IV} = 15.4$. Departure

from inertial scaling at this time occurs in both the DNS and LBM-LES models, although the velocity then goes on to decay at a rate between the theoretical laws for the inertial and viscous phases. This may be due to the fact that the Reynolds number for case 4, $Re_b = 5000$, is very close to the critical Reynolds number of $Re_{cr} = 3170$, corresponding to a case with a Froude number of $Fr = 0.42$. The critical Reynolds number is the threshold above which the current will transition from the slumping phase to the inertial phase, and below which the current will bypass the inertial phase, transitioning directly into the viscous phase. In cases where $Re_b \gg Re_{cr}$ or $Re_b \ll Re_{cr}$, closer agreement is observed with the viscous scaling laws.

For case 2, where $Re_b = 1000$, the transition to the viscous phase occurs at $\tilde{t} \approx 10$ in the Nek5000 DNS model. The scaling laws predict a direct transition from the slumping to viscous phase at $\tilde{t}_{SV} = 11.2$, in reasonable agreement with the DNS output. Following the transition, front velocity in the DNS model scales according to the $\tilde{u}_f \propto \tilde{t}^{-3/2}$ law as expected. The predictions of RAFSINE and VirtualFluids are in close agreement with the DNS result, both in the time of transition to the viscous phase and the subsequent decay in velocity. However, significant disparities are observed between the DNS result and the experimental and numerical predictions of Ottolenghi *et al.*⁴³ The front velocity in the experiment declines to a constant value of $\tilde{u}_f = 0.36$, before transitioning to the viscous phase at $\tilde{t} \approx 20$, much later than the transition time predicted by the scaling laws or observed in the DNS. The results of two experimental runs conducted by Amy *et al.*⁷¹ for Reynolds numbers of 950 and 1280 are also plotted for reference. The Amy *et al.*⁷¹ experiments also transition at $\tilde{t} \approx 20$, indicating that the Ottolenghi *et al.*⁴³ result is not an anomaly, although there is a wide spread between the experimental front velocities post-transition. The 3D LBM-LES simulation of Ottolenghi *et al.*⁴³ also follows this trend. It is proposed that the difference between the DNS and experimental result is caused by greater turbulence generation in physical experiments relative to the DNS and LBM-LES simulations. Around the transitional Reynolds number, the experimental result may be more sensitive to additional sources of turbulence generation in the experiments, such as surface roughness, and disturbance triggered by the gate release, which makes the idealized DNS model a poorer representation of the experimental conditions. A review of the other cases shows that at higher Reynolds numbers ($Re_b \geq 5000$), the results of DNS simulations are in good agreement with experiments.

The front velocity results for case 5 are presented in Fig. 7(c). In case 5, $Re_b = 8950$, the front velocity predictions of RAFSINE and VirtualFluids are validated against the DNS simulations of Cantero *et al.*¹⁸ The transition times predicted by the Cantero *et al.*¹⁸ DNS model are in very close agreement with the scaling laws, which predict $\tilde{t}_{SI} = 12.7$ and $\tilde{t}_{IV} = 19.8$. Additionally, the scaling laws are a very good quantitative prediction of front velocity. Both RAFSINE and Virtual fluids show good agreement with the Cantero *et al.*¹⁸ correctly predicting transition times and scaling within each phase. An experimental result of Marino *et al.*,⁷² experimental run 3 ($Re_b = 8620$), was also plotted for reference. The sparsity in front velocity readings makes direct comparison challenging, but the transition time to the inertial phase is in reasonable agreement with the Cantero *et al.*¹⁸ DNS model and LBM-LES simulations, although the onset of the viscous phase appears to occur later in the Marino *et al.*⁷² experimental run.

In case 6 [Fig. 7(d)], $Re_b = 10\,000$, the results of RAFSINE and VirtualFluids are very similar, both showing good agreement with the scaling law predictions of $\tilde{t}_{SI} = 12.7$ and $\tilde{t}_{IV} = 19.8$. The LBM model of Ottolenghi *et al.*⁴³ shows good agreement with the scaling laws in the slumping and inertial phase, but does not transition to the viscous phase at the expected time. The experimental current of Ottolenghi *et al.*⁴³ appears to begin a transition to the inertial phase at $\tilde{t} \approx 12$, and then front velocity plateaus, before decaying according to the inertial scaling law until $\tilde{t} \approx 30$. A similar trend is observed in the experimental run B0-1 of Amy *et al.*,⁷¹ $Re_b = 11\,400$, although the onset of viscous scaling occurs at a later time due to the higher Reynolds number.

For case 7 [Fig. 7(e)], $Re_b = 15\,000$, the front velocity predictions of RAFSINE and VirtualFluids are validated against the DNS simulation of Cantero *et al.*²¹ The transition times in the Cantero *et al.*²¹ DNS results are again in very close agreement with the scaling laws, which predict transition to the inertial and viscous phases at $\tilde{t}_{SI} = 12.7$ and $\tilde{t}_{IV} = 24.7$. The LBM-LES models demonstrate good agreement with the DNS result, accurately predicting both phase transition times and scaling within the phases. Figure 7(e) also includes plots from the $Re_b = 15\,550$ experiment of Marino *et al.*,⁷² and the $Re_b = 15\,700$ experiment of Huppert and Simpson.¹⁰ To the extent that either the RAFSINE or VirtualFluids simulation deviates from the DNS, they remain within the range of front velocities spanned by the two experimental results, indicating the models still offer a high degree of accuracy.

Case 8 [Fig. 7(f)], $Re_b = 30\,000$, is beyond the range of DNS, but the predictions of the LBM-LES models can be validated against the experiments of Huppert and Simpson¹⁰ and Ottolenghi *et al.*⁴³ Additionally, it is possible to compare performance against the finite-volume NS-LES model of Pelmard *et al.*,³⁴ who ran a lock-exchange simulation for $Re_b = 28\,284$. Since the experiment of Huppert and Simpson¹⁰ and simulation of Pelmard *et al.*³⁴ have lock-lengths of $\tilde{x}_0 > 1$, it is necessary to rescale velocity and time such that $\tilde{u}_f/(\tilde{h}_0)^{1/2} = u_f/(g'h_0)^{1/2}$ and $\tilde{t}(\tilde{h}_0)^{1/2}/\tilde{x}_0 = t(g'h_0)^{1/2}/x_0$, causing the transition to the inertial phase to collapse down to the same time regardless of lock-length, as outlined in Sec. I. Both experimental results show close agreement with the scaling law prediction of $\tilde{t}_{SI}(\tilde{h}_0)^{1/2}/\tilde{x}_0 = 11.0$. The RAFSINE simulation transitions prematurely but shows close agreement with the experiments and scaling laws in the inertial phase. VirtualFluids and the NS-LES model of Pelmard *et al.*³⁴ transition closer to $\frac{\tilde{t}_{SI}(\tilde{h}_0)^{1/2}}{\tilde{x}_0} = 11$, but the Pelmard *et al.*³⁴ simulation decays more rapidly post transition. Both LBM-LES models displayed an equivalent degree of accuracy to the conventional NS-LES model of Pelmard *et al.*,³⁴ in the prediction of front velocity and phase transition in lock-exchange gravity currents.

Insight into the internal dynamics of the gravity current can be gained from a review of the spanwise averaged density contours ($\bar{\rho}$) through time for case 8, presented in Fig. 8. The RAFSINE and VirtualFluids contours of $\bar{\rho}$ in case 8 both display the development of spanwise coherent, Kelvin-Helmholtz instability induced, billows at early times ($\tilde{t} \leq 5$). Although these billows have been observed to undergo substantial growth in 2D simulations, it is anticipated that in a 3D simulation of a turbulent current, the billows will lose their

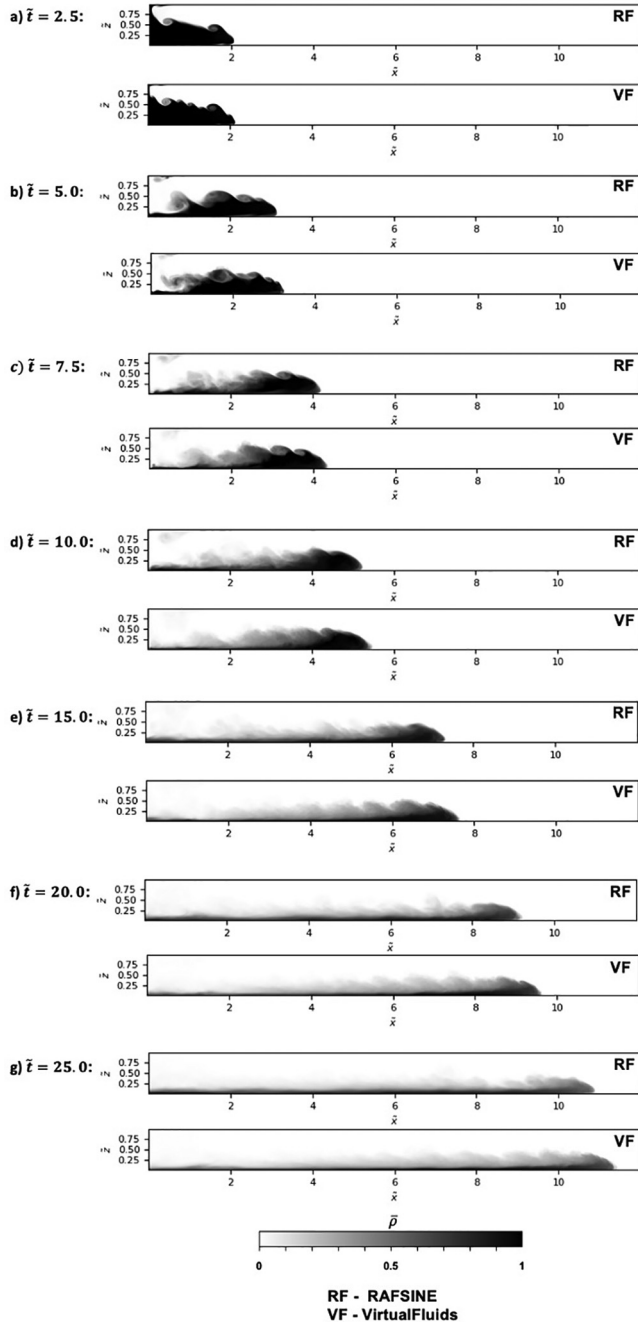


FIG. 8. Contour plots of spanwise averaged density in LBM-LES simulations of case 8, $Re_b = 30\,000$, run in RAFSINE and VirtualFluids. Contours are plotted at times (a) $\tilde{t} = 2.5$, (b) $\tilde{t} = 5.0$, (c) $\tilde{t} = 7.5$, (d) $\tilde{t} = 10.0$, (e) $\tilde{t} = 15.0$, (f) $\tilde{t} = 20.0$, and (g) $\tilde{t} = 25.0$.

spanwise coherence with time due to spanwise perturbations in the chaotic flow field.^{18,20,21,43} This process occurs in both LBM-LES models, with spanwise coherence of the Kelvin-Helmholtz billows disintegrating in the simulations by $\tilde{t} = 10$.

B. Near-wall region

In this section, the ability of the RAFSINE and VirtualFluids models to capture the near-wall flow characteristics of a saline gravity current is assessed by validation against DNS data from Cantero *et al.*²¹ and the Nek5000 simulations. Accurate prediction of the flow properties in the near-wall region is necessary for simulating a number of important physical processes in environmental gravity current flows, such as turbulence production due to lower boundary shear stresses, as well as erosion and deposition of stationary material at the boundaries.

Accurate simulation of near-wall flow requires a high level of near-wall resolution, which is measured by the non-dimensional distance (z^+) of the wall adjacent nodes from a no-slip boundary. The distance from a wall adjacent node to the boundary (Δz_1) is non-dimensionalized by friction velocity (u_τ), and kinematic viscosity (ν), as shown in Eq. (60). The friction velocity (u_τ) is defined in Eq. (61), where τ_w is the wall shear stress, calculated using Eq. (62),

$$z^+ = \frac{\tilde{u}_\tau \Delta \tilde{z}_1}{\tilde{\nu}}, \tag{60}$$

$$\tilde{u}_\tau = \sqrt{\tilde{\tau}_w / \tilde{\rho}}, \tag{61}$$

$$\tilde{\tau}_w = \tilde{\mu} \left. \frac{\partial \tilde{u}}{\partial \tilde{z}} \right|_{wall}. \tag{62}$$

The velocity gradient at the lower boundary $\left. \frac{\partial \tilde{u}}{\partial \tilde{z}} \right|_{wall}$ is calculated via a second-order accurate finite difference approximation at the wall, using the fluid velocity at the two nearest fluid nodes in the \hat{e}_z direction. A schematic of near-wall grid spacing in Nek5000, RAFSINE, and VirtualFluids is presented in Fig. 9. The Nek5000 discretization has a wall node where $\mathbf{u} = 0$, and the two nearest fluid nodes in the \hat{z} direction are at spacings of $\Delta \tilde{z}_1$, and $\Delta \tilde{z}_2 > \Delta \tilde{z}_1$ as grid spacing is non-uniform in the vertical direction. In the LBM-LES models, the boundary is located at a distance $\Delta \tilde{z}_1 = \Delta \tilde{x} / 2$ from the nearest fluid node due to the use of the halfway bounce-back boundary condition.⁴⁴ The second fluid node is then spaced at a distance of $\Delta \tilde{x}$ from the wall adjacent node. As the Nek5000 DNS simulation has a non-uniform grid spacing in the vertical direction, and a larger number of mesh points relative to the LBM-LES models, the fluid nodes used in the Nek5000 velocity gradient approximations span a smaller z^+ range.

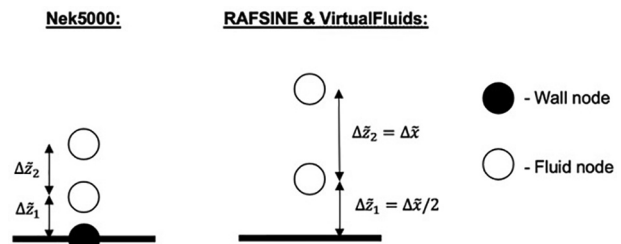


FIG. 9. Schematic of near-wall grid spacing in Nek5000, RAFSINE, and VirtualFluids.

TABLE III. Maximum z^+ of wall-adjacent node in all numerical simulations.

Case No.	Re_b	Max z^+ of wall-adjacent node		
		RAFSINE	VirtualFluids	Nek5000
1	895	0.57	0.60	...
2	1 000	0.56	0.59	0.11
3	3 450	1.53	2.10	...
4	5 000	1.80	2.75	0.10
5	8 950	2.83	4.45	...
6	10 000	2.89	4.68	...
7	15 000	3.83	5.98	...
8	30 000	4.45	6.92	...

Pelmard *et al.*,³⁴ who investigated grid resolution requirements for wall-resolved LES simulations of gravity currents, recommend that the maximum z^+ of a wall-adjacent node must meet the criteria $z^+ < 10$ to sufficiently capture the boundary layer. The maximum z^+

of wall-adjacent nodes, presented in Table III, shows that this standard is met in all cases. Further to this condition, the maximum z^+ is within the viscous sublayer of the current's boundary layer, $z^+ \leq 5$, in all cases but cases 7 and 8 in VirtualFluids, where z^+ lies just within the buffer region $5 < z^+ < 30$. Overall, the range of maximum z^+ values is equivalent to that used by Pelmard *et al.*,³⁴ who reported $2.5 < z_{\max}^+ < 7$ across their simulations.

Verification of the maximum z^+ requires the calculation of the non-dimensional wall shear stress ($\bar{\tau}_w$), which has been validated against DNS for cases $\in \{2, 4, 7\}$. The validation of the $\bar{\tau}_w$ predictions of the LBM-LES models against DNS of case 2, $Re_b = 1000$, is presented in Fig. 10, where contour plots of $\bar{\tau}_w$ at $\tilde{t} = 8$ and $\tilde{t} = 20$ are presented in Figs. 10(a) and 10(b), respectively.

At $\tilde{t} = 8$, the stress pattern in the DNS result is characterized by a region of high stress along the current front, followed by a fairly uniform stress distribution in the body, and very low shear stresses in the region behind the removed gate. There is a gradual increase in stress ahead of the front due to the displacement of ambient fluid by the flow. By $\tilde{t} = 20$, two lobes have formed at the head, and the peaks in shear stress occur along the edges of the lobes. Behind the head, the

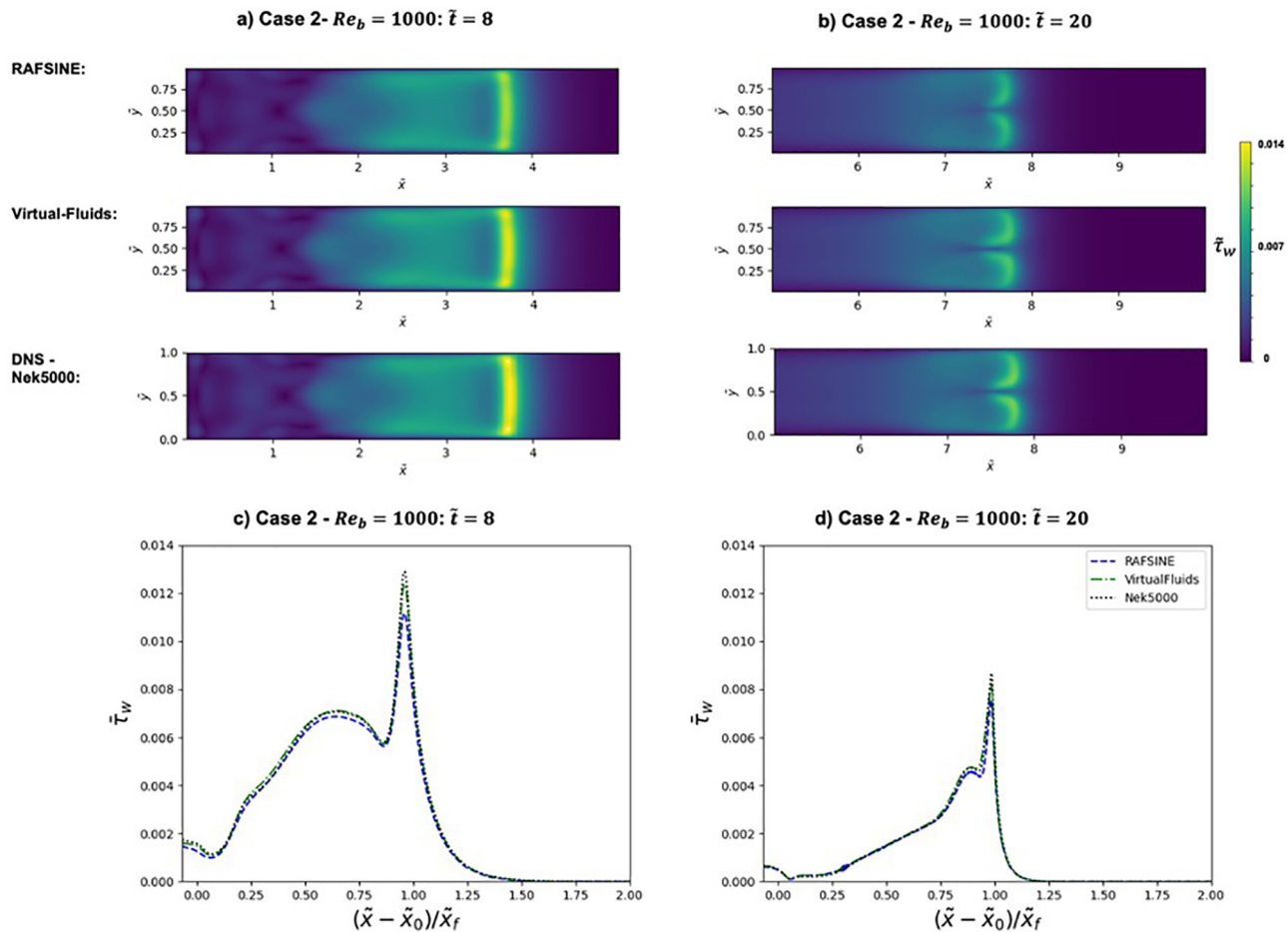


FIG. 10. Validation of predicted dimensionless shear stress on the lower boundary of the RAFSINE the VirtualFluids simulations against the Nek5000 DNS result for case 2, $Re_b = 1000$. (a) Contours of $\bar{\tau}_w$ on the lower boundary at $\tilde{t} = 8$. (b) Contours of $\bar{\tau}_w$ on the lower boundary at $\tilde{t} = 20$. (c) Plot of spanwise averaged shear stress ($\bar{\tau}_w$) at $\tilde{t} = 8$. (d) Plot of spanwise averaged shear stress ($\bar{\tau}_w$) at $\tilde{t} = 20$.

spanwise stress distribution is relatively uniform but steadily decreases with distance from the head. Stresses ahead of the front are lower at $\tilde{t} = 20$ as fluid is displaced less rapidly, due to the deceleration of the current in the viscous phase. The stress distributions predicted by RAFSINE and VirtualFluids are both in very close agreement with the DNS contours.

A more quantitative validation can be conducted by comparing plots of spanwise averaged wall shear stress $\bar{\tau}_w = \frac{1}{L_2} \int_0^{L_2} \tau_w d\tilde{y}$, presented in Figs. 10(c) and 10(d) for $\tilde{t} = 8$ and $\tilde{t} = 20$, respectively. Shear stress is plotted against the rescaled streamwise distance $(\tilde{x} - \tilde{x}_0)/\tilde{x}_f$, where \tilde{x}_f is the front location predicted by a given numerical model at $\tilde{t} \in \{8, 20\}$. This has the effect of collapsing the location of the front $(\tilde{x} - \tilde{x}_0 = \tilde{x}_f)$ to $(\tilde{x} - \tilde{x}_0)/\tilde{x}_f = 1$ on the graphs, which filters out errors in predicted front location in the LBM-LES models, allowing the stream-wise profiles of $\bar{\tau}_w$ to be compared relative to the front of each current.

The $\bar{\tau}_w$ distribution in the DNS result exhibits a sharp spike in shear stress at the current front, followed by a smaller rounded peak in the body, after which stress decreases with distance from the head. Profiles of $\bar{\tau}_w$ in RAFSINE and VirtualFluids show close quantitative agreement with the DNS result in the locations of peak $\bar{\tau}_w$, although VirtualFluids appears to perform better in predicting the magnitude of the peak stress. This is reflected in the e_{L_1} error in the total frictional force (F_w) applied to the lower boundary, defined in Eqs. (63)–(64), where $\tilde{t}_i \in \{\tilde{t}_1, \tilde{t}_2, \dots, \tilde{t}_{N_t}\}$ is a list of $N_t = 12$ times at which a results file was output,

$$e_{L_1} = \frac{1}{N_t} \sum_i \left| \frac{F_w^{DNS}(\tilde{t}_i) - F_w^{LBM-LES}(\tilde{t}_i)}{F_w^{DNS}(\tilde{t}_i)} \right|, \quad (63)$$

$$F_w(\tilde{x}, \tilde{y}, \tilde{t}_i) = \int_0^{\tilde{L}_2} \int_0^{\tilde{L}_1} \tau_w(\tilde{x}, \tilde{y}, \tilde{t}_i) d\tilde{x} d\tilde{y}. \quad (64)$$

In case 2, the e_{L_1} error in RAFSINE and VirtualFluids was 6.9% and 1.9%, respectively, demonstrating that although both models show good agreement with the DNS result, the error in the VirtualFluids prediction is less than a third of the RAFSINE model error.

Contours of $\bar{\tau}_w$ in the RAFSINE, VirtualFluids and Nek5000 simulations of case 4 are presented in Figs. 11(a) and 11(b) at $\tilde{t} = 8$ and $\tilde{t} = 20$, respectively. At $\tilde{t} = 8$, the DNS contours display peaks in shear stress at the lobes of the current front, followed by a roughly circular region of high stress within the body. This secondary peak in stress is less evident at $\tilde{t} = 20$, where the high stress regions are concentrated at the head. The qualitative stress distribution is well reproduced in RAFSINE and VirtualFluids, as both display high stresses at the current front, and a second circular high stress region in the body at $\tilde{t} = 8$. However, the contours indicate that the peaks in stress are lower in the RAFSINE model than in the DNS result. This is confirmed by the plots of spanwise averaged shear stress in Figs. 11(c) and 11(d). Although the qualitative structure of the $\bar{\tau}_w$ profile is captured by RAFSINE, the magnitude of the peaks is substantially lower than the DNS result. The magnitude of the peak stress in the VirtualFluids result is in close agreement with the DNS at $\tilde{t} = 8$, but is underpredicted at $\tilde{t} = 20$. This is evident in the e_{L_1} errors for case 4, where the VirtualFluids model has an error of 4.9%, still in good agreement with DNS, while the RAFSINE model error was 33.4%. This reflects a known limitation of the standard Smagorinsky turbulence model in

the near wall region when simulating turbulent flows.^{34,36} As C_s is held constant, see Sec. II C 1, the eddy viscosity may be non-zero in the near-wall region, which reduces the velocity gradient at the wall, thereby decreasing $\bar{\tau}_w$ and artificially increasing the thickness of the boundary layer. Although this can be overcome through the use of Van Driest style damping or a dynamic Smagorinsky model, researchers often use the standard Smagorinsky model when concerned with capturing flow features far from the wall.^{34,36,38,43} As outlined in Sec. II C 1, the VirtualFluids LBM formulation does not include a sub-grid eddy-viscosity turbulence model, and so is not impacted by this limitation.

Similar trends are observed in case 7 (Fig. 12). In this case, the contour plots of $\bar{\tau}_w$, Figs. 12(a) and 12(b), are compared to those produced by Cantero *et al.*,²¹ which unfortunately were published without a color scale, making direct comparison challenging. However, the streaking stress patterns in the head, clearly observable in the DNS result, are reproduced in both RAFSINE and VirtualFluids, as well as a banded region of high stress in the body at $\tilde{t} = 8$. The stress distribution in RAFSINE is noticeably smoother than that observed in the Cantero *et al.*²¹ DNS result and VirtualFluids, which is due to the previously discussed spurious damping in the near-wall region caused by the standard Smagorinsky model. Plots of $\bar{\tau}_w$, Figs. 12(c) and 12(d), show that RAFSINE substantially underpredicts shear stresses, while the VirtualFluids profile shows reasonable quantitative agreement, although still marginally underpredicting the frontal peak in stress. As Cantero *et al.*²¹ do not provide quantitative stress data for the lower boundary, but does provide plots of $\bar{\tau}_w$ at $\tilde{t} = 8$ and $\tilde{t} = 20$, the e_{L_1} error is calculated using the spanwise averaged frictional force on the wall (\bar{F}_w), as shown in Eqs. (65) and (66), where $\tilde{t}_i \in \{8, 20\}$. Using this revised definition, the e_{L_1} error in RAFSINE becomes substantial at 50.6%, while the VirtualFluids model remains in good agreement with DNS at 8.8%

$$e_{L_1} = \frac{1}{N_t} \sum_i \left| \frac{\bar{F}_w^{DNS}(\tilde{t}_i) - \bar{F}_w^{LBM-LES}(\tilde{t}_i)}{\bar{F}_w^{DNS}(\tilde{t}_i)} \right|, \quad (65)$$

$$\bar{F}_w(\tilde{x}, \tilde{t}_i) = \int_0^{\tilde{L}_1} \bar{\tau}_w(\tilde{x}, \tilde{t}_i) d\tilde{x}. \quad (66)$$

In a modeling scenario where close quantitative agreement with DNS is essential, errors could be reduced through the application of hierarchical grids to increase resolution in the near wall region.⁵⁷

C. Computational performance of the LBM-GPU framework

As outlined in Sec. II C, the LBM-LES codes are accelerated by exporting computations to a GPU at each time step, rather than completing the tasks on the CPU. The core motivation for shifting to this LBM-GPU framework is that GPU acceleration reduces the elapsed time of a simulation relative to an equivalent implementation that runs exclusively on CPUs. However, direct comparison between the computational performance of CPU and GPU implementations is complicated by the fact that they run on different hardware using different data structures, and to the authors' knowledge, consensus on a suitable metric has not been established.

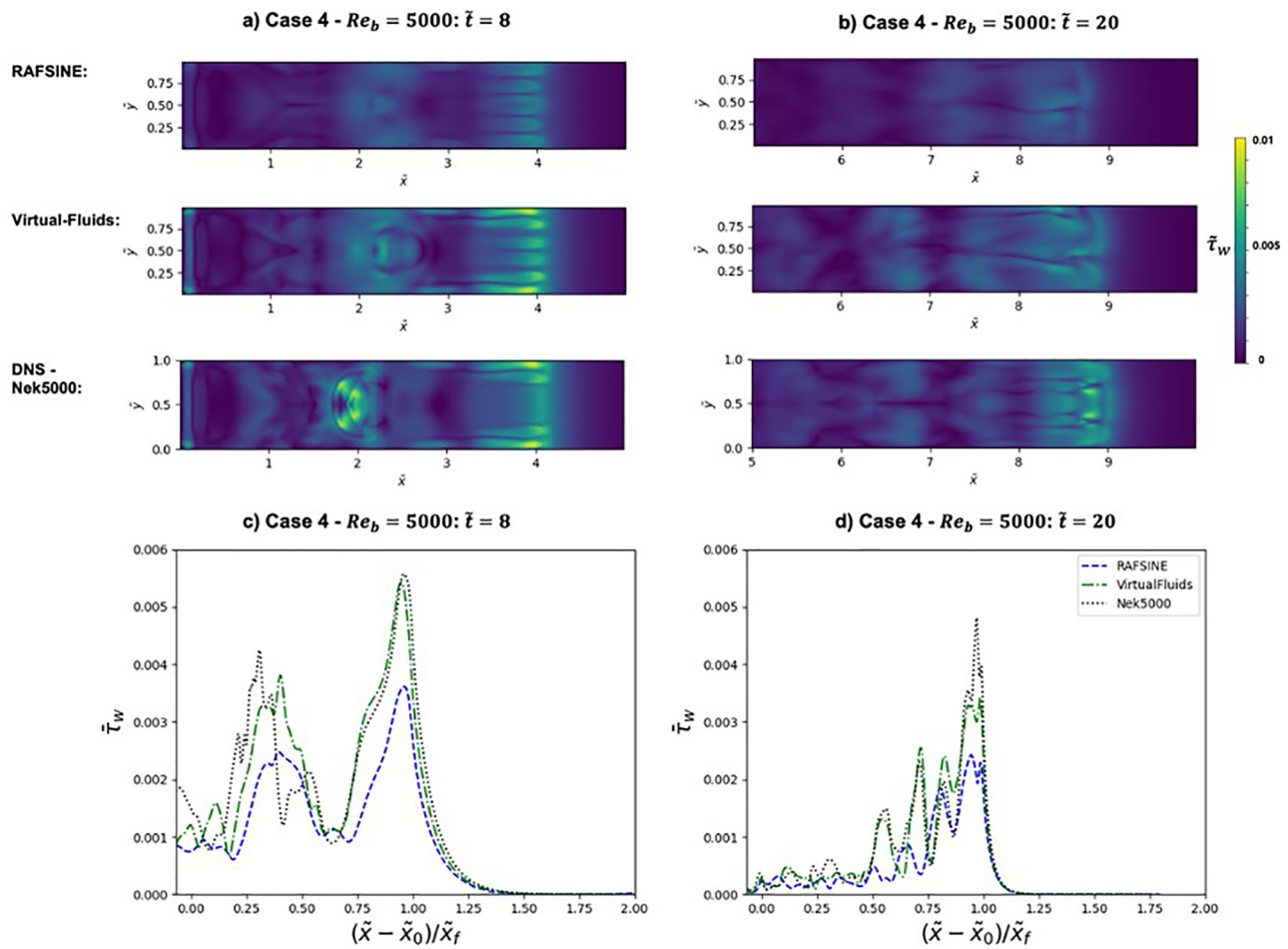


FIG. 11. Validation of predicted dimensionless shear stress on the lower boundary of the RAFSINE the VirtualFluids simulations against the Nek5000 DNS result for case 4, $Re_b = 5000$. (a) Contours of $\bar{\tau}_w$ on the lower boundary at $\tilde{t} = 8$. (b) Contours of $\bar{\tau}_w$ on the lower boundary at $\tilde{t} = 20$. (c) Plot of spanwise averaged shear stress ($\bar{\tau}_w$) at $\tilde{t} = 8$. (d) Plot of spanwise averaged shear stress ($\bar{\tau}_w$) at $\tilde{t} = 20$.

When comparing the performance of two numerical models implemented to run across CPU cores, the total CPU time (T_{CPU}) of each program, that is, the total time taken to process instructions, would be used to measure the computational cost of the numerical models. The relationship between $T_{CPU} = \sum_{i,j} t_{P_j}^i$ and elapsed time is illustrated in Fig. 13(a), where $t_{P_j}^i$ is a single block of processing time on one of n processors $P_j \in \{P_1, P_2, \dots, P_n\}$. It seems appropriate to extend this metric of total CPU time to comparisons between conventional NS models written to run on CPUs and LBM implementations in which the CPU exports computations to a GPU.

In both RAFSINE and VirtualFluids, total CPU time is approximately equal to elapsed time, as the programs are executed on a single CPU core that exports data to the GPU device, as illustrated in Fig. 13(b). Therefore, observed speedups in total CPU time as a result of the GPU acceleration will not translate directly into equivalent speedups in elapsed time relative to a NS model running exclusively on CPU cores. The realized reduction in elapsed time will depend upon the number of cores used to run the

CPU code, the efficiency of the parallel implementation, and the time taken for input/output operations.

Using this framework, the speedup offered by the GPU-accelerated LBM-LES codes relative to DNS in Nek5000 has been evaluated by comparing both total CPU time and elapsed time at low Reynolds numbers ($Re_b \leq 5000$). The Nek5000 simulations were run on ARC4, part of the High-Performance Computing facilities at the University of Leeds, UK. Compute nodes on the cluster contain two Intel Xeon Gold 6138 CPUs (“Sky Lake”), each with 20 cores, a clock rate for non-AVX instructions of 2.0 GHz, and are connected with InfiniBand EDR of 100Gbit/s. The $Re_b = 1000$ and $Re_b = 5000$ Nek5000 simulations were run across 100 and 250 cores, respectively. In the LBM-LES codes, computations were exported to an NVIDIA V100 Tensor Core GPU.

The speedups in T_{CPU} and T_E are presented in Table IV, where times are written in the format h:min:s. Both RAFSINE and VirtualFluids reduce total processing time relative to Nek5000 by a factor of 10^2 for the $Re_b = 1000$ simulation, and $10^{2.6}$ for the $Re_b = 5000$ case. This translates to a reduction in elapsed time of $10^{1.2}$

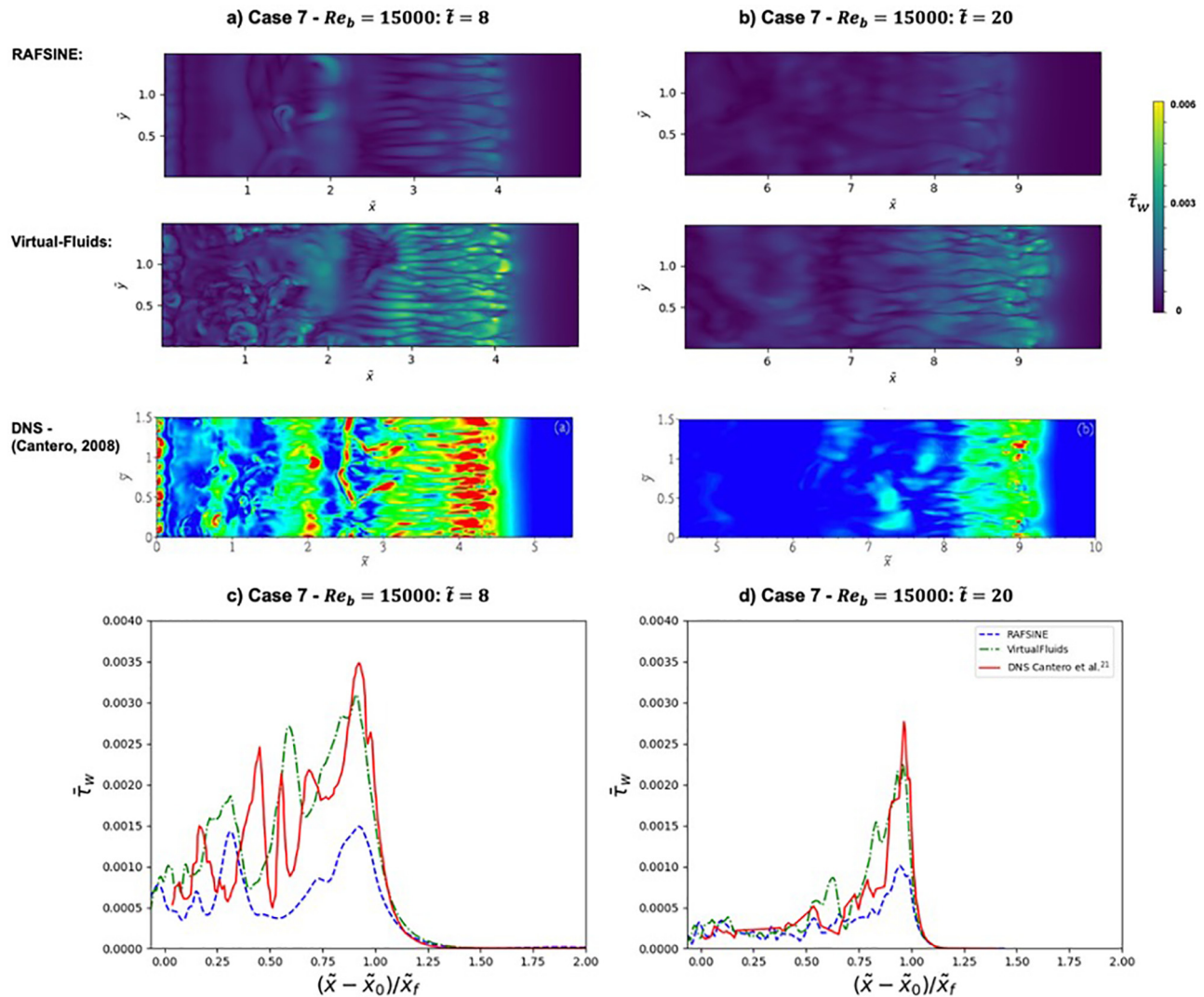


FIG. 12. Validation of predicted dimensionless shear stress on the lower boundary of the RAFSINE the VirtualFluids simulations against Cantero *et al.*²¹ result for case 7, $Re_b = 15000$. (a) Contours of $\bar{\tau}_w$ on the lower boundary at $\tilde{t} = 8$. (b) Contours of $\bar{\tau}_w$ on the lower boundary at $\tilde{t} = 20$. (c) Plot of spanwise averaged shear stress ($\bar{\tau}_w$) at $\tilde{t} = 8$. (d) Plot of spanwise averaged shear stress ($\bar{\tau}_w$) at $\tilde{t} = 20$.

and 10^2 for the respective cases, demonstrating significant speedups relative to DNS can be achieved while preserving accuracy in the prediction of key flow properties.

A comparison is also made to the computational cost of the NS-LES simulations of Pelmaid *et al.*,³⁴ who used the structured non-staggered finite-volume code described by Norris⁷³ and which has been applied to a wide range of problem types.^{74–76} Pelmaid *et al.*³⁴ ran simulations on a computing cluster at New Zealand eScience Infrastructure (NeSI) consortium, consisting of nodes with two Intel Xeon E5–2680 Sandy Bridge 2.70 GHz CPUs, each with eight cores. Pelmaid *et al.*³⁴ report the total CPU time required to run a turbulent lock-exchange gravity current simulation, with a standard Smagorinsky sub-grid turbulence model, across a range of grid sizes. Simulations on the largest meshes were run across 128 cores, while 64 cores were used for the

smaller grids. Their results are taken to be representative of the typical cost associated with modern NS-LES codes.

The total CPU time required to simulate a unit of non-dimensional time ($\tilde{t} = \tilde{t}(\tilde{h}_0)^{1/2}/\tilde{x}_0 = t(g'h_0)^{1/2}/x_0$) in RAFSINE, VirtualFluids, and the Pelmaid *et al.*³⁴ study is presented in Fig. 14. Total CPU times for the LBM-LES models are presented for grid sizes of $N_{nodes} \in \{15, 37.5, 42.2\} \times 10^6$, as this represents the full range of grid sizes used in the present study. The comparison indicates that the LBM-GPU framework reduces total processing time by a factor of approximately 10^3 , when contrasted with the representative total CPU time of the finite-volume NS-LES framework. Assuming a speedup due to multi-core CPU parallelization similar to that achieved by Nek5000, it is anticipated that this would translate into a reduction in

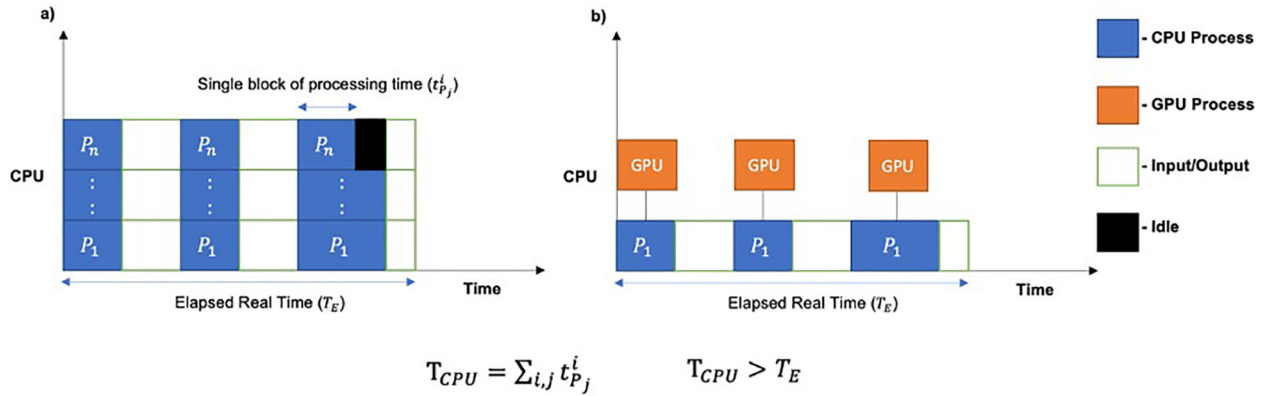


FIG. 13. Schematic of total CPU time as it relates to (a) CPU implementations, and (b) GPU accelerated implementations.

TABLE IV. Speedup in total CPU time and elapsed time of LBM-LES models relative to DNS in Nek5000. Times are presented in the format h:min:s.

Case No.	Re_b	Nek5000		RAFSINE			VirtualFluids		
		T_{CPU}	T_E	$T_{CPU} (\approx T_E)$	Speedup		$T_{CPU} (\approx T_E)$	Speedup	
					T_{CPU}	T_E		T_{CPU}	T_E
2	1000	39:21:13	07:53:47	00:23:48	$10^{2.0}$	$10^{1.3}$	00:26:52	$10^{1.9}$	$10^{1.2}$
4	5000	173:27:33	43:29:44	00:25:05	$10^{2.6}$	$10^{2.0}$	00:27:00	$10^{2.6}$	$10^{2.0}$

T_E by a factor of approximately 10^2 , when contrasted with the Pelmard *et al.*³⁴ code running across 128 cores on the NeSI cluster. This conclusion is in agreement with the findings of a similar analysis conducted by King *et al.*⁷⁷ Additionally, the LBM-GPU framework offers substantial performance advantages relative to the CPU implementation of Ottolenghi *et al.*,⁴³ which has enabled 3D simulations at higher Reynolds numbers.

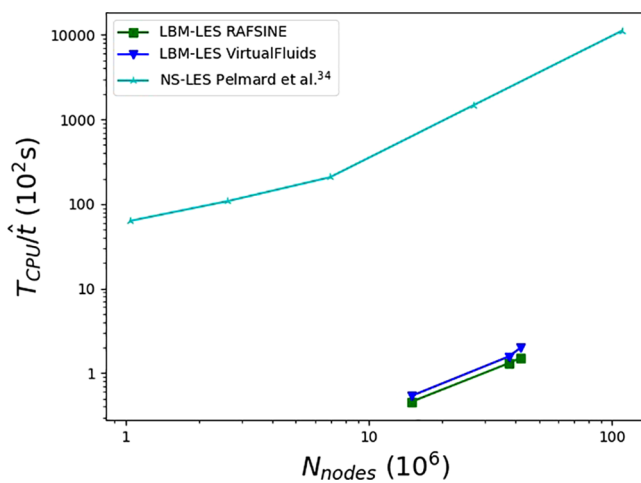


FIG. 14. Total CPU time per unit of non-dimensional time \hat{t} in RAFSINE, VirtualFluids, and finite-volume LES simulations of Pelmard *et al.*³⁴

The results in Table IV and Fig. 14 show that both RAFSINE and VirtualFluids achieve similar speedups. The standard metric for comparing the performance of two LBM-GPU codes is the number of node updates per second, typically reported in the millions, i.e., MNUPS. When running on an NVIDIA V100 GPU, RAFSINE and VirtualFluids report average update rates of 1307 MNUPS and 1064 MNUPS, respectively. RAFSINE has been robustly optimized by Delbosc *et al.*⁴⁹ to run simulations in rectilinear domains, such as a lock-exchange channel. However, a direct comparison of the efficiency of the GPU implementations cannot be made since VirtualFluids uses two $D3Q27$ lattices for the f_{ijk} and Φ_{ijk} distributions, which demands more memory resources and computations than the $D3Q19$ and $D3Q6$ lattices used by RAFSINE. Additionally, the cumulant collision kernel requires more computations per time step than the BGK collision kernel. The marginal performance gap could be narrowed by the integration of the cumulant and FCM kernels, as this would eliminate redundant memory accesses caused by reading and writing distribution functions to calculate the same macroscopic variables in each kernel.

IV. CONCLUSIONS

In the present study, two LBM-LES models of lock-exchange gravity currents are validated against high-resolution simulations and experiments with regard to their ability to capture key qualitative and quantitative features of a lock-exchange gravity current flow across a wide range of Reynolds numbers. The two codes, RAFSINE and VirtualFluids, demonstrate equivalent accuracy to conventional NS-LES solvers in predictions of front velocity in the slumping, inertial,

and viscous phases of the flow. Additionally, the VirtualFluids model achieved good agreement with DNS in the prediction of shear stress on the lower boundary.

The computational performance of the LBM-GPU framework was assessed relative to the computational cost of DNS run in Nek5000 and that reported for the finite-volume NS-LES simulations of Pelmard *et al.*³⁴ It is demonstrated that the LBM-GPU framework delivers speedups of at least one order of magnitude in the elapsed real time of a simulation relative to DNS at low Reynolds numbers ($Re \leq 5000$), and speedups of three orders of magnitude in total CPU time relative to a NS-LES model across a range of grid sizes for a fully turbulent flow.

Given the speedup that can typically be achieved through multi-core CPU parallelization of CFD codes, it is estimated that the LBM-GPU models reduce the elapsed time required for a simulation by two orders of magnitude while demonstrating equivalent accuracy. As a result, the numerical modeling framework presented herein can be used as a foundation for the development of models that capture more of the complexity of gravity currents, such as the two-way coupling between the hydrodynamics of environmental scale flows and the morphodynamics of boundaries in channels with complex geometries. This modeling objective would otherwise be too challenging to attempt due to the computational expense of conventional NS-LES codes.

ACKNOWLEDGMENTS

This work was supported by the Engineering and Physical Sciences Research Council (EPSRC) Centre for Doctoral Training in Fluid Dynamics grant EP/L01615X/1 for the University of Leeds; and the Turbidites Research Group consortium (AkerBP, CNOOC, ConocoPhillips, Murphy, OMV, and Oxy). The funders had no role in study design; the collection, analysis, and interpretation of data; or in the preparation of the article and decision to publish. This work was undertaken on ARC4, part of the High-Performance Computing facilities at the University of Leeds, UK.

AUTHOR DECLARATIONS

Conflict of Interest

The authors have no conflicts to disclose.

DATA AVAILABILITY

The data that support the findings of this study are available within the article.

REFERENCES

- W. J. Schmitz, "On the interbasin-scale thermohaline circulation," *Rev. Geophys.* **33**, 151, <https://doi.org/10.1029/95RG00879> (1995).
- R. M. Dorrell, J. Peakall, C. Burns, and G. M. Keevil, "A novel mixing mechanism in sinuous seafloor channels: Implications for submarine channel evolution," *Geomorphology* **303**, 1–12 (2018).
- J. Penney and M. Stastna, "Direct numerical simulation of double-diffusive gravity currents," *Phys. Fluids* **28**, 086602 (2016).
- E. Meiburg and B. Kneller, "Turbidity currents and their deposits," *Annu. Rev. Fluid Mech.* **42**, 135 (2010).
- M. G. Wells and R. M. Dorrell, "Turbulence processes within turbidity currents," *Annu. Rev. Fluid Mech.* **53**, 59 (2021).
- B. M. Bates, N. Andreini, and C. Ancey, "Basal entrainment by Newtonian gravity-driven flows," *Phys. Fluids* **28**, 053101 (2016).
- M. E. Negretti, F. L. Tucciarone, and A. Wirth, "Intruding gravity currents and re-circulation in a rotating frame: Laboratory experiments," *Phys. Fluids* **33**, 096607 (2021).
- D. Paoli, "Influence of reservoir properties on the dynamics of a migrating current of carbon dioxide," *Phys. Fluids* **33**, 016602 (2021).
- D. Tritton, *Physical Fluid Dynamics* (Cambridge University Press, 1977).
- H. E. Huppert and J. Simpson, "The slumping of gravity currents," *J. Fluid Mech.* **99**, 785 (1980).
- T. Von Karman, "The engineer grapples with nonlinear problems," *Bull. Am. Math. Soc.* **46**, 615 (1940).
- T. B. Benjamin, "Gravity currents and related phenomena," *J. Fluid Mech.* **31**, 209 (1968).
- J. W. Rottman and J. E. Simpson, "Gravity currents produced by instantaneous releases of a heavy fluid in a rectangular channel," *J. Fluid Mech.* **135**, 95 (1983).
- J. A. Fay, *Oil Sea* (Springer US, 1969), pp. 53–63.
- D. P. Hoult, "Oil spreading on the sea," *Annu. Rev. Fluid Mech.* **4**, 341 (1972).
- A. Hogg, "Lock-release gravity current and dam-break flows," *J. Fluid Mech.* **569**, 61 (2006).
- H. E. Huppert, "The propagation of two-dimensional and axisymmetric viscous gravity currents over a rigid horizontal surface," *J. Fluid Mech.* **121**, 43 (1982).
- M. Cantero, J. Ryong Lee, S. Balachandar, and M. H. García, "On the front velocity of gravity currents," *J. Fluid Mech.* **586**, 1–39 (2007).
- E. Meiburg, S. Radhakrishnan, and M. Nasr-Azadani, "Modeling gravity and turbidity currents: computational approaches and challenges," *Appl. Mech. Rev.* **67**, 040802 (2015).
- C. Härtel, E. Meiburg, and F. Necker, "Analysis and direct numerical simulation of the flow at a gravity-current head. Part 1. Flow topology and front speed for slip and no-slip boundaries," *J. Fluid Mech.* **418**, 189 (2000).
- M. I. Cantero, S. Balachandar, M. H. García, and D. Bock, "Turbulent structures in planar gravity currents and their influence on the flow dynamics," *J. Geophys. Res.* **113**, 004645, <https://doi.org/10.1029/2007JC004645> (2008).
- L. F. R. Espath, L. C. Pinto, S. Laizet, and J. H. Silvestrini, "Two- and three-dimensional direct numerical simulation of particle-laden gravity currents," *Comput. Geosci.* **63**, 9 (2014).
- L. F. R. Espath, L. C. Pinto, S. Laizet, and J. H. Silvestrini, "High-fidelity simulations of the lobe-and-cleft structures and the deposition map in particle-driven gravity currents," *Phys. Fluids* **27**, 56604 (2015).
- E. P. Francisco, L. F. R. Espath, and J. H. Silvestrini, "Direct numerical simulation of bi-disperse particle-laden gravity currents in the channel configuration," *Appl. Math. Modell.* **49**, 739 (2017).
- C. R. Marshall, R. M. Dorrell, S. Dutta, G. M. Keevil, J. Peakall, and S. M. Tobias, "The effect of Schmidt number on gravity current flows: The formation of large-scale three-dimensional structures," *Phys. Fluids* **33**, 106601 (2021).
- Z. He, L. Zhao, R. Zhu, and P. Hu, "Separation of particle-laden gravity currents down a slope in linearly stratified environments," *Phys. Fluids* **31**, 106602 (2019).
- O. E. Sequeiros, A. Cantelli, E. Viparelli, J. D. L. White, M. H. García, and G. Parker, "Modeling turbidity currents with nonuniform sediment and reverse buoyancy," *Water Resour. Res.* **45**, W06408, <https://doi.org/10.1029/2008WR007422> (2009).
- S. Abd El-Gawad, A. Cantelli, C. Pirmez, D. Minisini, Z. Sylvester, and J. Imran, "Three-dimensional numerical simulation of turbidity currents in a submarine channel on the seafloor of the Niger Delta slope," *J. Geophys. Res.* **117**, C05026, <https://doi.org/10.1029/2011JC007538> (2012).
- S.-U. Choi and M. H. Garca, "k- ϵ turbulence modeling of density currents developing two dimensionally on a slope," *J. Hydraul. Eng.* **128**, 55 (2002).
- A. Arfaie, *Numerical Modelling of the Influence of Lower Boundary Roughness on Turbulent Sedimentary Flows* (University of Leeds, 2015).
- R. W. Kelly, *Seafloor Gravity Currents: Flow Dynamics in Overspilling and Sinuous Channels* (University of Leeds, 2018).
- R. W. Kelly, R. M. Dorrell, A. D. Burns, and W. D. McCaffrey, "The structure and entrainment characteristics of partially confined gravity currents," *J. Geophys. Res.* **124**, 014042, <https://doi.org/10.1029/2018JC014042> (2019).
- J. Smagorinsky, "General circulation experiments with the primitive equations," *Mon. Weather Rev.* **91**, 99 (1963).

- ³⁴J. Pelma, S. Norris, and H. Friedrich, "LES grid resolution requirements for the modelling of gravity currents," *Comput. Fluids* **174**, 256 (2018).
- ³⁵S. K. Ooi, G. Constantinescu, and L. J. Weber, "2D large-eddy simulation of lock-exchange gravity current flows at high Grashof numbers," *J. Hydraul. Eng.* **133**, 1037 (2007).
- ³⁶S. K. Ooi, G. Constantinescu, and L. Weber, "Numerical simulations of lock-exchange compositional gravity current," *J. Fluid Mech.* **635**, 361 (2009).
- ³⁷G. Constantinescu, "LES of lock-exchange compositional gravity currents: A brief review of some recent results," *Environ. Fluid Mech.* **14**, 295 (2014).
- ³⁸J. Pelma, S. Norris, and H. Friedrich, "Statistical characterisation of turbulence for an unsteady gravity current," *J. Fluid Mech.* **901**, 7 (2020).
- ³⁹K. Steenhauer, T. Tokyay, and G. Constantinescu, "Dynamics and structure of planar gravity currents propagating down an inclined surface," *Phys. Fluids* **29**, 036604 (2017).
- ⁴⁰C. K. Aidun and J. R. Clausen, "Lattice-Boltzmann method for complex flows," *Annu. Rev. Fluid Mech.* **42**, 439 (2010).
- ⁴¹Z. Guo, B. Shi, and C. Zheng, "A coupled lattice BGK model for the Boussinesq equations," *Int. J. Numer. Methods Fluids* **39**, 325 (2002).
- ⁴²L. Rocca, C. Adduce, V. Lombardi, G. Sciortino, and R. Hinkelmann, "Development of a lattice Boltzmann method for two-layered shallow-water flow," *Int. J. Numer. Methods Fluids* **70**, 1048 (2012).
- ⁴³L. Ottolenghi, P. Prestinini, A. Montessori, C. Adduce, and L. Rocca, "Lattice Boltzmann simulations of gravity currents," *Eur. J. Mech.-B* **67**, 125 (2018).
- ⁴⁴T. Krüger, H. Kusumaatmaja, A. Kuzmin, O. Shardt, G. Silva, and E. M. Viggien, *The Lattice Boltzmann Method* (Springer, 2017).
- ⁴⁵N. Delbosc, *Real-Time Simulation of Indoor Air Flow Using the Lattice Boltzmann Method on Graphics Processing Unit* (University of Leeds, 2015).
- ⁴⁶M. Junk, A. Klar, and L. S. Luo, "Asymptotic analysis of the lattice Boltzmann equation," *J. Comput. Phys.* **210**, 676 (2005).
- ⁴⁷F. Dubois, "Equivalent partial differential equations of a lattice Boltzmann scheme," *Comput. Math. Appl.* **55**, 1441 (2008).
- ⁴⁸P. L. Bhatnagar, E. P. Gross, and M. Krook, "A model for collision processes in gases. I. Small amplitude processes in charged and neutral one-component systems," *Phys. Rev.* **94**, 511 (1954).
- ⁴⁹N. Delbosc, J. L. Summers, A. I. Khan, N. Kapur, and C. J. Noakes, "Optimized implementation of the lattice Boltzmann method on a graphics processing unit towards real-time fluid simulation," *Comput. Math. Appl.* **67**, 462 (2014).
- ⁵⁰S. Hou, J. Sterling, S. Chen, and G. D. Doolen, "A lattice Boltzmann subgrid model for high Reynolds number flows," arXiv:comp-gas/9401004 (1994).
- ⁵¹H. Liu, C. Zou, B. Shi, Z. Tian, L. Zhang, and C. Zheng, "Thermal lattice-BGK model based on large-eddy simulation of turbulent natural convection due to internal heat generation," *Int. J. Heat Mass Transfer* **49**, 4672 (2006).
- ⁵²X. Yang, Y. Mehmani, W. A. Perkins, A. Pasquali, M. Schönherr, K. Kim, M. Perego, M. L. Parks, N. Trask, M. T. Balhoff, M. C. Richmond, M. Geier, M. Krafczyk, L. S. Luo, A. M. Tartakovsky, and T. D. Scheibe, "Intercomparison of 3D pore-scale flow and solute transport simulation methods," *Adv. Water Resour.* **95**, 176 (2016).
- ⁵³M. Geier, A. Greiner, and J. G. Korvink, "A factorized central moment lattice Boltzmann method," *Eur. Phys. J. Spec. Top.* **171**, 55 (2009).
- ⁵⁴M. Geier, M. Schönherr, A. Pasquali, and M. Krafczyk, "The cumulant lattice Boltzmann equation in three dimensions: Theory and validation," *Comput. Math. Appl.* **70**, 507 (2015).
- ⁵⁵M. Geier, A. Pasquali, and M. Schönherr, "Parametrization of the cumulant lattice Boltzmann method for fourth order accurate diffusion part I: Derivation and validation," *J. Comput. Phys.* **348**, 862 (2017).
- ⁵⁶M. Geier, S. Lenz, M. Schönherr, and M. Krafczyk, "Under-resolved and large eddy simulations of a decaying Taylor–Green vortex with the cumulant lattice Boltzmann method," *Theor. Comput. Fluid Dyn.* **35**, 169 (2021).
- ⁵⁷M. Geier, A. Pasquali, and M. Schönherr, "Parametrization of the cumulant lattice Boltzmann method for fourth order accurate diffusion part II: Application to flow around a sphere at drag crisis," *J. Comput. Phys.* **348**, 889 (2017).
- ⁵⁸M. Geier and M. Schönherr, "Esoteric twist: An efficient in-place streaming algorithm for the lattice Boltzmann method on massively parallel hardware," *Computation* **5**, 19 (2017).
- ⁵⁹H. Alihussain, M. Geier, and M. Krafczyk, "A parallel coupled lattice Boltzmann-volume of fluid framework for modeling porous media evolution," *Materials* **14**, 2510 (2021).
- ⁶⁰NEK5000 Version 19.0, Release date - 12/28/2019, Argonne National Laboratory, Illinois. available: <https://nek5000.mcs.anl.gov>.
- ⁶¹A. T. Patera, "A spectral element method for fluid dynamics: Laminar flow in a channel expansion," *J. Comput. Phys.* **54**, 468 (1984).
- ⁶²P. F. Fischer, *Implementation Considerations for the OIFS/Characteristics Approach to Convection Problems* (Argonne National Laboratory, 2003).
- ⁶³H. Alihussain, *Massively Parallel Simulations of Chemical Dissolution in Porous Media Based on Advanced Lattice Boltzmann Models* (Technische Universität Braunschweig, 2020).
- ⁶⁴F. Kyrousi, A. Leonardi, F. Roman, V. Armenio, F. Zanello, J. Zordan, C. Juez, and L. Falcomer, "Large Eddy Simulations of sediment entrainment induced by a lock-exchange gravity current," *Adv. Water Resour.* **114**, 102 (2018).
- ⁶⁵J. Hacker, P. F. Linden, and S. B. Dalziel, "Mixing in lock-release gravity currents," *Dyn. Atmos. Oceans* **24**, 183 (1996).
- ⁶⁶G. Keulegan, *Thirteenth Progress Report on Model Laws for Density Currents: An Experimental Study of the Motion of Saline Water from Locks into Fresh Water Channels* (US Department of Commerce, National Bureau of Standards, 1957).
- ⁶⁷J. E. Simpson, "Effects of the lower boundary on the head of a gravity current," *J. Fluid Mech.* **53**, 759 (1972).
- ⁶⁸C. J. Lloyd, J. Peakall, A. D. Burns, G. M. Keevil, R. M. Dorrell, P. B. Wignall, and T. M. Fletcher, "Hydrodynamic efficiency in sharks: The combined role of riblets and denticles," *Bioinspiration Biomimetics* **16**, 046008 (2021).
- ⁶⁹V. Luan Ho, *Multi-Pulsed Turbidity Current Dynamics and Geological Implications* (University of Leeds, 2018).
- ⁷⁰F. G. Serchi, J. Peakall, D. B. Ingham, and A. D. Burns, "A numerical study of the triggering mechanism of a lock-release density current," *Eur. J. Mech.-B* **33**, 25 (2012).
- ⁷¹L. A. Amy, A. J. Hogg, J. Peakall, and P. J. Talling, "Abrupt transitions in gravity currents," *J. Geophys. Res.* **110**, 3001, <https://doi.org/10.1029/2004JF000197> (2005).
- ⁷²B. M. Marino, L. P. Thomas, and P. F. Linden, "The front condition for gravity currents," *J. Fluid Mech.* **536**, 49 (2005).
- ⁷³S. Norris, *Finite Volume Differencing Schemes* (University of Sydney, 2000).
- ⁷⁴T. Hattori, S. E. Norris, M. P. Kirkpatrick, and S. W. Armfield, "Prandtl number dependence and instability mechanism of the near-field flow in a planar thermal plume," *J. Fluid Mech.* **732**, 105 (2013).
- ⁷⁵N. Williamson, S. W. Armfield, M. P. Kirkpatrick, and S. E. Norris, "Transition to stably stratified states in open channel flow with radiative surface heating," *J. Fluid Mech.* **766**, 528 (2015).
- ⁷⁶R. C. Storey, J. E. Cater, and S. E. Norris, "Large eddy simulation of turbine loading and performance in a wind farm," *Renewable Energy* **95**, 31 (2016).
- ⁷⁷M. F. King, A. Khan, N. Delbosc, H. L. Gough, C. Halios, J. F. Barlow, and C. J. Noakes, "Modelling urban airflow and natural ventilation using a GPU-based lattice-Boltzmann method," *Build. Environ.* **125**, 273 (2017).
- ⁷⁸J. Tölke and M. Krafczyk, "TeraFLOP computing on a desktop PC with GPUs for 3D CFD," *Int. J. Comput. Fluid Dyn.* **22**, 443 (2008).
- ⁷⁹M. Schönherr, K. Kucher, M. Geier, M. Stiebler, S. Freudiger, and M. Krafczyk, "Multi-thread implementations of the lattice Boltzmann method on non-uniform grids for CPUs and GPUs," *Comput. Math. Appl.* **61**, 3730 (2011).
- ⁸⁰N. Delbosc, D. Adekanye, and A. Khan, RAFSINE, NVIDIA GPU with minimum compute capability 3.0, CMake (minimum version 3.15), C++ compiler with C++14 support, minimum CUDA Version 9.0, Paraview, C++, CUDA, Ref. 49, 2014, https://github.com/scda-FluidsCDT/Saline_Gravity_Current_Models/tree/main/Straight_Channel_Single_Release_Lock_Exchange/RAFSINE.
- ⁸¹Institute for Computational Modeling in Civil Engineering (iRMB), VirtualFluids, NVIDIA GPU with minimum compute capability 3.0, CMake (minimum version 3.15), C++ compiler with C++14 support, C++, CUDA, minimum CUDA Version 9.0, Paraview, Refs. 78 and 79, 2008, <https://git.rz.tu-bs.de/irmb/virtualfluids>.
- ⁸²Argonne National Laboratory, Nek5000-v19.0, FORTRAN, 2017, https://github.com/scda-FluidsCDT/Saline_Gravity_Current_Models/tree/main/Straight_Channel_Single_Release_Lock_Exchange/Nek5000.